

The fluid dynamics of work transfer in the non-uniform viscous rotating flow within a Tesla disc turbomachine

Abhijit Guha^{a)} and Sayantan Sengupta

*Mechanical Engineering Department, Indian Institute of Technology Kharagpur,
Kharagpur 721302, India*

(Received 31 May 2013; accepted 20 January 2014; published online 3 March 2014)

In this article, the fluid dynamics of work transfer within the narrow spacing (usually of the order of 100 μm) of multiple concentric discs of a Tesla disc turbomachine (turbine or compressor) has been analysed theoretically and computationally. Both the overall work transfer and its spatial development have been considered. It has been established that the work transfer mechanism in a Tesla disc turbomachine is very different from that in a conventional turbomachine, and the formulation of the Euler's work equation for the disc turbomachine contains several conceptual subtleties because of the existence of complex, three dimensional, non-uniform, viscous flow features. A work equivalence principle has been enunciated, which establishes the equality between the magnitudes of work transfer determined rigorously from two different approaches—one based on the shear stress acting on the disc surfaces and the other based on the change in angular momentum of the fluid. Care is needed in identifying the shear stress components that are responsible for the generation or absorption of useful power. It is shown from the Reynolds transport theorem that mass-flow-averaged tangential velocities (as opposed to the normally used area-averaged values) must be used in determining the change in angular momentum; the calculation has to be carefully formulated since both radial velocity (that determines throughput) and tangential velocity (that generates torque) depend strongly on the coordinate perpendicular to the disc surfaces. The principle of work transfer has been examined both in the absolute and relative frames of reference, revealing the subtle role played by Coriolis force. The concept of a new non-dimensional quantity called the torque potential fraction ($\Delta\tilde{H}$) is introduced. The value of $\Delta\tilde{H}$ at any radial position increases with a decrease in inter-disc spacing. The computational fluid dynamic analysis shows that, for small value of inter-disc spacing and high value of tangential speed ratio, most of the angular momentum of the fluid is transferred to the surfaces of the discs in the inlet region and correspondingly, the value of the torque potential fraction is very high even in the inlet region. On the other hand, for larger inter-disc spacing, the change in angular momentum in the radial direction is more uniformly distributed between the inlet and the outlet, and the value of the torque potential fraction increases gradually with decreasing radius. The complex (sometimes continuous, sometimes disjointed) three-dimensional shapes of the iso-surfaces of $U_\theta r$ (product of absolute tangential velocity and radius) have been shown, for the first time, which provide insight into the fluid dynamics of work transfer within corotating discs. © 2014 AIP Publishing LLC. [<http://dx.doi.org/10.1063/1.4866263>]

I. INTRODUCTION

The Euler's work equation is the most fundamental relation specifying the work transfer involved in a conventional turbomachine. Consequently it is discussed in all textbooks of turbomachines.¹⁻⁴

^{a)} Author to whom correspondence should be addressed. Electronic mail: a.guha@mech.iitkgp.ernet.in

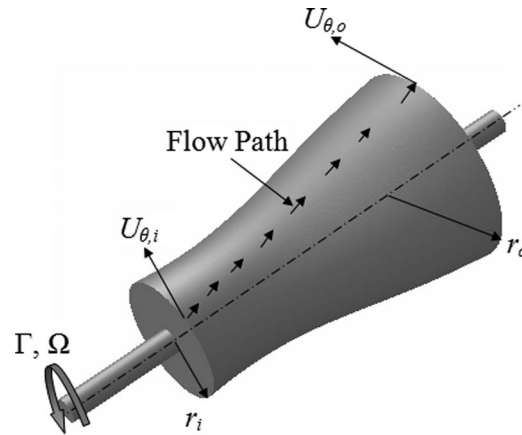


FIG. 1. Schematic diagram of a conventional turbomachine.

All textbooks give a diagram similar to Figure 1 and, for the specified configuration, deduce the Euler's equation:

$$\Gamma_{Euler} = \dot{m} (U_{\theta,o} r_o - U_{\theta,i} r_i), \quad (1)$$

where, \dot{m} is the mass flow rate, r is the radius, and U_θ is the absolute tangential velocity. The following convention for subscripts and superscripts is adopted in this paper: the subscripts i and o denote, respectively, the inlet and the outlet conditions; the subscripts r , θ , and z are used to denote the corresponding components of a vector quantity along the three cylindrical coordinates; the symbol overbar ($\bar{\quad}$) is used to denote the area-averaged value of a variable and the symbol hat ($\hat{\quad}$) is used to denote the mass-flow-averaged value of a variable. In Eq. (1) and throughout this paper, Γ is taken as the torque that is applied *on the fluid*, since this will help to develop a unified treatment of conventional turbomachines and Tesla disc turbomachines. From Newton's third law of motion, the torque that is applied on the solid body is equal and opposite to that applied on the fluid: $\Gamma_{solid} = -\Gamma_{fluid}$. The shaft power, \dot{W}_x , can be calculated from $\dot{W}_x = \Gamma_{solid} \Omega$, where, Ω is the rotational speed of the rotor; \dot{W}_x is positive for a turbine, \dot{W}_x is negative for a compressor.

In a conventional turbomachine, work transfer is carried out by the dynamic action of (usually many) blades. The flow of fluid around the aerofoil cross-section of a blade creates a pressure difference between the suction and pressure sides of the blade. The integrated effect of this pressure difference results in an aerodynamic force. The rotational motion of the rotor blades creates the required velocity along the line of action of the aerodynamic force for the transfer of power between the fluid stream and the rotor blades. The direction of the force and that of the rotational motion are such that power is transferred from the rotor blades to the fluid stream in a compressor and power is transferred from the fluid stream to the rotor blades in a turbine.

Unlike a conventional turbomachine in which the pressure distribution around the blades is responsible for the generation of the torque, shear stress acting on the disc surfaces gives rise to the torque in a Tesla disc turbine. There are other major differences in the flow features which will be revealed in the course of the present analysis. The present paper investigates whether the Euler's work transfer equation would be applicable for the very different type of fluid flow that exists in the Tesla disc turbine, and, if so, what would be the rigorous and generic form of the Euler's work equation. The fluid dynamics has been analysed here by mathematical theories as well as by the computational fluid dynamics (CFD) solutions to gain fundamental physical insight into both the overall work transfer and its spatial development. The details of the theory have been worked out for the flow configuration of a disc turbine but it has been shown that the principle and the developed equations are also applicable to disc pump or compressor.

The details of the working principle of a disc turbine are given in Refs. 5–13. Tesla turbine is a bladeless turbomachine in which the rotor is constructed by a series of co-axial, parallel flat

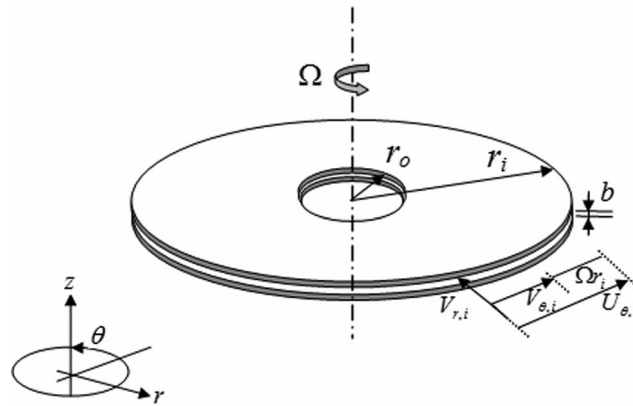


FIG. 2. Schematic diagram of the domain for the mathematical solution. [The gap within the two discs, in relation to the radius, is exaggerated in the sketch for clarity.]

discs. The discs are attached to a central shaft maintaining a small gap among one another. The combination of discs and shaft is placed inside a cylindrical casing with a small radial and axial clearance. The working fluid is injected nearly tangentially to the rotor by means of one or more inlet nozzles. There are exit ports near the shaft at the centre of each disc. Figure 2 shows a schematic diagram of two consecutive discs in a Tesla disc turbine which consists of many such discs. The discs are separated by an inter-disc-spacing b . The components of the velocity at the inlet are represented by arrows. For a Tesla turbine, subjected to a steady rotational speed Ω , the components of absolute velocity (r , z , and θ components of U) are related to the components of relative velocity (r , z , and θ components of V) by the following transformation:

$$U_r = V_r; \quad U_z = V_z; \quad U_\theta = (V_\theta + \Omega r). \quad (2)$$

Guha and Sengupta¹⁴ have shown the novelty in the fluid dynamics of the rotating flow within a Tesla disc turbine. Like the Batchelor flow¹⁵ or the Stewartson flow,¹⁶ the flow in the Tesla disc turbine also takes place within the gap between two discs. However, unlike the cases considered by Batchelor or Stewartson, the flow in Tesla turbine is not generated due to the rotation of the discs. The working fluid with both tangential and radial velocity enters through the small gap between the discs which are of finite radius. This rotating flow generates torque on the discs' surfaces which leads to the rotation of the rotor. The flow configuration is also different from that of Bödewadt,¹⁷ because Bödewadt had dealt with the case where there was a single static disc of infinite radius, the rotating fluid was of infinite expanse along the axis of rotation, and moreover there was no superposed inflow. The cases considered by some of the modern researchers like Poncet *et al.*¹⁸ with superposed outflow is not applicable for Tesla turbine because they had considered a stator-rotor system but all discs in a Tesla turbine are rotors and the superposed flow is inward. None of the solutions given by Holodniok *et al.*,^{19,20} is applicable for Tesla turbine because in all of their cases the discs are imparting rotation to the fluid. Another distinguishing feature of the Tesla turbine configuration is the small gap between two adjacent discs, which may be small enough in certain cases to be considered as a micro-channel. Usually, the two boundary layers on the two discs would merge together, so that a core flow of the Batchelor-type does not occur. The boundary layers near the discs cannot also be described like the Ekman layer in which only Coriolis component of the inertial terms is retained.

Hoya and Guha⁹ presented the design of a multipurpose flexible experimental rig and undertook a systematic series of experiments on the performance and efficiency of Tesla disc turbine. One important challenge is to measure low torque at very high angular speed. Several methods were tested and a new method called “the angular acceleration method” was developed. Tesla turbine has several important advantages.⁹ For example, the manufacturing cost of the discs would be lower than the aerofoil-shaped blades of conventional turbomachines. The turbine has self-cleaning nature

due the centrifugal force field. This makes it possible to operate the turbine with non-conventional fuels like biomass which produce solid particles.

The main disadvantage of the Tesla disc turbines is that the present values of their efficiency are lower than that of conventional turbines. However, it is hoped that the current surge of research would improve the efficiency of the disc turbines—Guha and Smiley,¹¹ for example, have developed an improved design of the nozzle, greatly improving the efficiency and achieving uniformity in the velocity profile of the jet. (The loss in the nozzle is generally recognized^{6,8} as a major source of loss in a conventional Tesla turbine.) Tesla turbines may find niche applications in the future. However, even if this does not happen on a commercial scale, the understanding of the fluid dynamics of this special type of rotating flow (as explained above) is important in its own right.

Many experimental Tesla disc turbines are built with one or more nozzles at the periphery of the rotor. The fluid velocity at the nozzle exit may be large leading to compressibility effects, including the presence of shock waves in some instances. If the fluid is a two-phase mixture, such as a solid-particle-laden gas, then the principles of two-phase flow²¹ and careful consideration of the concepts of total pressure and total temperature in two-phase flows^{22,23} may be necessary. The presence of a finite number of nozzles may introduce non-uniformity in inlet conditions for the disc rotors. This is why the generic principle of work transfer, that includes the effects of non-uniformity and compressibility, has been developed here.

The overall organization of the present paper is as follows. The general principle of Euler's work transfer equation for the flow through co-rotating discs is formulated in Sec. II. The formulation is capable of dealing with generic forms of non-uniformity in the flow-field (such as what would be the case if the inter-disc spacing is large or if a finite number of discrete nozzles is present at the inlet), and the flow may be incompressible or compressible, laminar or turbulent. Section II shows that the torque can be calculated from changes in angular momentum as well as from viscous shear stresses (the work equivalence principle), and not all shear stress components are responsible for the generation of useful power. After establishing the work equivalence principle in Sec. II, its validity is assessed in two complementary ways: analytically in Sec. III and by means of CFD simulations in Sec. V. The analytical theory is valid for small inter-disc spacing and axi-symmetric inlet condition. The CFD simulations are based on full Navier-Stokes equations, and can handle large inter-disc spacing and complex boundary conditions. New physical insight on the spatial development of work transfer has been obtained from the CFD simulations. Section IV addresses the form of the work transfer principle in stationary vis-à-vis rotating frames of reference. Additional physical reflections and limiting cases have been discussed in Secs. VI and VII.

II. FORMULATION OF EULER'S WORK EQUATION AND WORK EQUIVALENCE PRINCIPLE FOR TESLA DISC TURBOMACHINE

It has been explained in Sec. I that the nature of force producing the torque is different in conventional turbomachines and Tesla disc turbomachines (pressure vs shear force). Another major difference arises from the fact that the flow in Tesla disc turbomachine is severely non-uniform. The serious non-uniformity in the z -direction is caused by the action of viscosity and is accentuated because the dimension in the z -direction is very small (inter-disc-spacing b being very small). Thus the z -variations of U_θ and V_r (and of U_z when inter-disc-spacing is relatively large) are of critical importance. Similarly, the r -variations of the velocity components and pressure must be accounted for. In a conventional turbomachine, the Euler's work equation [Eq. (1)] is often applied⁴ for one-dimensional steady flow. For more realistic calculations, the blades may be sub-divided into a few segments and Eq. (1) may be applied to each segment using a quasi-one-dimensional approach. In the Tesla disc turbine, the existence of the strong non-uniformity in multiple directions compels one to integrate the complex flow features directly into the theoretical formulation as shown below. We have shown the mathematical derivation for the flow configuration of a disc turbine, the interpretation of the final equations for a disc pump or compressor is given in Sec. II D.

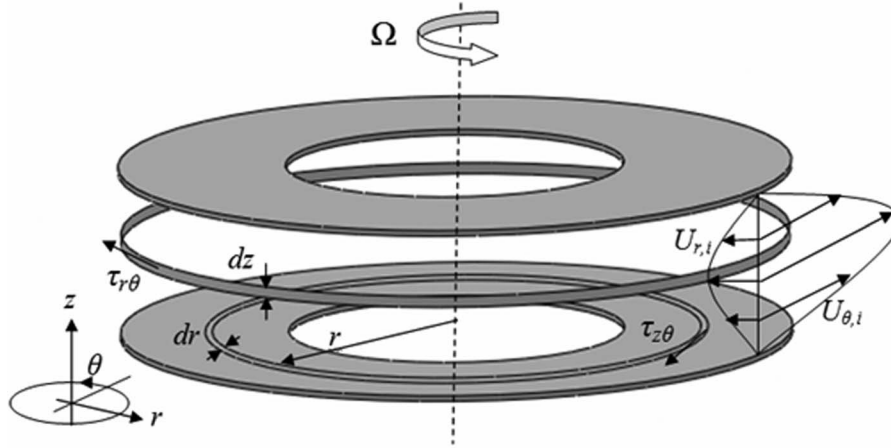


FIG. 3. Schematic morphology of non-uniform flow and orientation of shear stresses within a Tesla disc turbine. [Note the strong non-uniformity in the flow in two mutually perpendicular directions r and z . There may be additional non-uniformity in the θ direction for complex boundary conditions.]

A. Determination of angular momentum

Figure 3 depicts the flow domain and the control volume contains the fluid between two consecutive discs. The control surface consists of the inlet circumferential plane, the outlet circumferential plane, and the surfaces of the two discs.

Consider an elemental circumferential area $r d\theta dz$ at an arbitrary location (θ, z) at an arbitrary radius r . Mass flow rate through any circumferential plane (at arbitrary radius r) can be expressed as

$$\dot{m} = \int d\dot{m} = \int_0^b \int_0^{2\pi} \rho r |V_r| d\theta dz = r \int_0^b \int_0^{2\pi} \rho |V_r| d\theta dz. \quad (3)$$

In Steady flow, the same mass flow rate exists at inlet, outlet, and at any circumferential plane of arbitrary radius (between the inlet and the outlet). In incompressible flow ρ (density of the working fluid) can be taken outside the integral sign. Further, for axi-symmetric flow, $|V_r|$ can be taken outside the θ -integration. Therefore, for incompressible, axi-symmetric flow, Eq. (3) is simplified to

$$\dot{m} = 2\pi\rho r \int_0^b |V_r| dz.$$

Figure 3 shows that careful consideration of non-uniformity is needed in determining the flux of angular momentum at inlet. This is because the elemental mass flow rate depends on the radial velocity $V_{r,i}$ (which is strongly non-uniform in the z -direction) and this is to be multiplied by $U_{\theta,i}$ which is perpendicular to $V_{r,i}$ and is itself strongly non-uniform in the z -direction. There may be additional non-uniformity in the θ direction for complex boundary conditions.

The total flux of angular momentum at inlet ($r = r_i$) is given by

$$\begin{aligned} H_i &= \int U_{\theta,i} r_i d\dot{m} \\ &= r_i^2 \int_0^b \int_0^{2\pi} \rho U_{\theta,i} |V_{r,i}| d\theta dz. \end{aligned} \quad (4)$$

Equation (4) may be written in a more compact form if one defines the mass-flow-averaged absolute tangential velocity \hat{U}_θ as follows:

$$\hat{U}_\theta = \frac{\int_0^b \int_0^{2\pi} \rho U_\theta |V_r| d\theta dz}{\int_0^b \int_0^{2\pi} \rho |V_r| d\theta dz}. \quad (5)$$

For incompressible, axi-symmetric flow, Eq. (5) is simplified to $\hat{U}_\theta = \int_0^b U_\theta |V_r| dz / \int_0^b |V_r| dz$. Combining Eqs. (4) and (5) one obtains

$$H_i = \dot{m}_i r_i \hat{U}_{\theta,i}, \quad (6)$$

where, $\hat{U}_{\theta,i}$ is the mass-flow-averaged absolute tangential velocity at inlet.

Similarly, the flux of angular momentum at outlet is given by

$$H_o = \dot{m}_o r_o \hat{U}_{\theta,o}. \quad (7)$$

The Reynolds transport theorem^{24–26} applying on any system property (here, the property is H and its specific value is h) for a non-deforming control volume can be written as

$$\frac{d}{dt}(H_{sys}) = \int_{cv} \frac{\partial}{\partial t}(h\rho)dv + \int_{cs} h\rho(\vec{V} \cdot \vec{n})dA. \quad (8)$$

In Eq. (8), the term $\int_{cs} h\rho(\vec{V} \cdot \vec{n})dA$ signifies the net flux of angular momentum that can cross the control surface of the control volume. Out of four control surfaces the flux of angular momentum can enter or exit the control volume from the inlet circumferential plane and the outlet circumferential plane. Considering the sign convention of the direction normal (\vec{n}),

$$\int_{cs} h\rho(\vec{V} \cdot \vec{n})dA = - \int_{inlet} h(\rho |V_r| dA) + \int_{outlet} h(\rho |V_r| dA) = -H_i + H_o. \text{ Under steady flow oper-}$$

ating condition, $\int_{cv} \frac{\partial}{\partial t}(h\rho)dv = 0$. According to Newton's second law of motion, $\frac{d}{dt}(H_{sys})$ [in

Eq. (8)] is equal to the torque applied on the fluid i.e. Γ_{Euler} . Therefore, for the present study Eq. (8) can be expressed as

$$\Gamma_{Euler} = -H_i + H_o. \quad (9)$$

B. Determination of viscous torque

The control surfaces are such that pressure does not create any moment about the z -axis; the moment on the fluid control volume for the Tesla disc turbine is solely created by viscous shear forces. Out of the six independent elements of the symmetric stress tensor, only two shear stresses, viz., $\tau_{z\theta}$ and $\tau_{r\theta}$, act on the control surfaces such that they can produce a moment about the rotational axis z (see Figure 3). Consider a circular strip of width dr at a radius r on the surface of the disc. The shear stress acting on the strip is $\tau_{z\theta}(z=0)$. The shear force acting on the strip is $(rdr) \int_0^{2\pi} \tau_{z\theta}(z=0) d\theta$, and the moment of this force about z -axis is $(r^2 dr) \int_0^{2\pi} \tau_{z\theta}(z=0) d\theta$.

The total torque produced on the disc surface is $\int_{r_i}^{r_o} r^2 \int_0^{2\pi} \tau_{z\theta}(z=0) d\theta dr$. This torque should be multiplied by 2 since there are two such surfaces in the control volume. Now, consider a circular strip of height dz at an arbitrary z on the inlet plane. The total moment of the shear force acting on the inlet plane is $r_i^2 \int_0^b \int_0^{2\pi} \tau_{r\theta}(r=r_i) d\theta dz$. Similarly, the total moment of the shear force acting on the outlet plane is $-r_o^2 \int_0^b \int_0^{2\pi} \tau_{r\theta}(r=r_o) d\theta dz$. The total moment produced by the shear forces on all control surfaces can therefore be generally written for the Tesla disc turbine as

$$\Gamma_{shear} = 2 \int_{r_i}^{r_o} r^2 \int_0^{2\pi} \tau_{z\theta}(z=0) d\theta dr + r_i^2 \int_0^b \int_0^{2\pi} \tau_{r\theta}(r=r_i) d\theta dz - r_o^2 \int_0^b \int_0^{2\pi} \tau_{r\theta}(r=r_o) d\theta dz. \quad (10)$$

The shear stresses $\tau_{z\theta}$ and $\tau_{r\theta}$ are to be treated as algebraic quantities and a consistent sign convention must be used. $\tau_{r\theta}$ may be positive over some values of z , while it may be negative at other values of z .

It is interesting to note that both $\tau_{z\theta}$ and $\tau_{r\theta}$ create viscous torque *on the fluid* and thus need to be considered in the formulation of work equivalence principle. On the other hand, only $\tau_{z\theta}$ applies on the disc surface and thus only this component is responsible for the transfer of useful power that can be externally extracted from the shaft connected to the discs.

An order of magnitude analysis¹³ shows that the contribution of $\tau_{r\theta}$ would be small (since $r \gg z$) in comparison to that of $\tau_{z\theta}$. Hence $\tau_{r\theta}$ has been neglected in the analytical theory given in Sec. III below. In the CFD solution given in Sec. V, however, when a uniform velocity profile is prescribed at the inlet, the z -profile of U_θ forms rapidly and approaches the parabolic profile (for small aspect ratio and air as working fluid) assumed in the analytical theory within the first few grid points in the r -direction. Hence although the value of $\tau_{r\theta}$ is globally small (as expected from the order of magnitude analysis mentioned previously), $\tau_{r\theta}$ may not be small at the inlet surface where it matters most for the calculation of the applied viscous torque. However, the contribution of $\tau_{r\theta}$ to the applied viscous torque still remains small even in the CFD simulation because the surface area ($2\pi r_i b$) over which $\tau_{r\theta}$ acts is much smaller than the surface area over which $\tau_{z\theta}$ acts. In a practical Tesla disc turbine with one or more nozzles arranged around the circumference, there may be viscous stress generated in the shear layer between the rotating fluid and the stagnant fluid near the casing—this may be a physical reason for the existence of $\tau_{r\theta}$ in such flow configurations.

C. Work equivalence principle

The work equivalence principle for a Tesla disc turbomachine may be enunciated as: “The change in angular momentum of the fluid passing through a Tesla disc turbine is equal to the viscous torque applied at the boundary of the control volume.” Mathematically,

$$\Gamma_{Euler} = \Gamma_{shear}. \quad (11)$$

The validity of Eq. (11) has been assessed in Secs. III–V. In Sec. III A, the synopsis of an analytical theory is given, from which the three-dimensional, axi-symmetric flow field can be determined. Based on this analytically determined flow field, both Γ_{Euler} and Γ_{shear} can be calculated: the validity of Eq. (11) can then be checked. This is done in Sec. III B. In Sec. IV, additional physical insight is provided by analyzing the equations in the absolute and relative frames of reference: this, in particular, clarifies the subtle role played by the Coriolis force. In Sec. V, detailed CFD solutions are presented. This serves two purposes: the first utility is to assess the validity of Eq. (11) using the full Navier-Stokes equations for generalized geometries such as large aspect ratio (the analytical theory is based on several simplifying approximations), and the second use of the CFD solutions is to enhance the physical understanding.

D. Turbine versus pump or compressor

Although the fluid dynamics of work transfer has been developed above for the flow configuration of a Tesla disc turbine, the principle, and equations are equally applicable to disc pump or compressor as well. Thus Eqs. (9)–(11) are applicable for all types of disc turbomachines.

For a disc turbine, $H_o < H_i$. Equation (9) then shows that Γ_{Euler} is negative, which means that \dot{W}_x is positive. The reverse is true for disc pumps or compressors: $H_o > H_i$, Γ_{Euler} is positive and \dot{W}_x is negative.

Equation (11) demands that the sign of Γ_{shear} in disc turbines must also be opposite to that in disc pumps and compressors. This is physically satisfied by the fact that, for a disc turbine, the fluid imparts rotation to the disc and thus the tangential velocity of the disc is lower than the tangential velocity of the fluid adjacent to the disc ($\partial U_\theta / \partial z > 0$). For a disc pump or compressor, the disc imparts rotation to the fluid and thus the tangential velocity of the disc is greater than the tangential velocity of the fluid adjacent to the disc ($\partial U_\theta / \partial z < 0$). The sign of $\tau_{z\theta}$ in disc turbine is thus opposite to that in disc pump or compressor.

III. ANALYTICAL DEMONSTRATION OF THE WORK EQUIVALENCE PRINCIPLE, EQ. (11)

It is to be remembered that the work equivalence principle, Eq. (11) derived above, is valid for laminar as well as for turbulent flow. For laminar flow, the validity of Eq. (11) is assessed with the help of a simple analytical theory giving the velocity and pressure fields within a Tesla disc turbine.¹³ The essence of the analytical theory is given in Sec. III A for ready reference. Laminar flow is considered for the example calculations given in the present paper since the chosen disc turbine dimensions and flow conditions are such that the experiments in Ref. 10 established that the flow is laminar even for the largest inter-disc spacing considered here.

There are various works (e.g., Refs. 8 and 27) to suggest that the flow through co-rotating discs of a Tesla turbomachine may also become turbulent. The instability criteria for the flow over a rotating disc in an infinite expanse of fluid and for the flow between a static and a rotating disc are considered, respectively, by Lingwood^{28,29} and Cousin-Ritemard *et al.*³⁰ Cousin-Ritemard *et al.*³⁰ have found that the onset of instability occurs when the value of $\Omega b^2 / \nu$ exceeds 2000. The value of $\Omega b^2 / \nu$ considered in the present analysis is much less than 2000. However, the flow configuration of a stator-rotor assembly is different from that of a Tesla disc turbine (as explained in Sec. I), and there is a need for a detailed stability analysis for the present case, as noted by Rice⁸: “It is desirable that it be explored further both experimentally and by additional hydrodynamic stability analysis.”

A. Synopsis of an analytical theory for determining the flow field

The domain for the mathematical solution is the three-dimensional space (Figure 2) between two circular rotor discs separated axially (i.e., in the z -direction) by a distance b . The rotor inlet is situated along the periphery of the discs (i.e., at radius r_i). The rotor outlet is at the centre of the discs (at radius r_o).

The flow between the discs has been assumed to be steady, incompressible, laminar, and axisymmetric. Guha and Sengupta¹³ presented a detailed order of magnitude analysis of the various terms of the three-dimensional conservation equations in the cylindrical coordinate system and based on these the appropriate important terms for the present problem are included in the governing equations given below.

The continuity equation, the momentum equations, and boundary conditions are written in terms of relative velocities. For this purpose the relations between the absolute and relative velocities (Eq. (2)) are used. For small aspect ratio, the governing conservation equations take the following form:

$$\text{Continuity equation} \quad \frac{\partial V_r}{\partial r} + \frac{V_r}{r} = 0, \quad (12)$$

$$\theta - \text{Momentum equation} \quad V_r \frac{\partial V_\theta}{\partial r} + \frac{V_r V_\theta}{r} + 2\Omega V_r = \nu \frac{\partial^2 V_\theta}{\partial z^2}, \quad (13)$$

$$r - \text{Momentum equation} \quad V_r \frac{\partial V_r}{\partial r} - \Omega^2 r - 2\Omega V_\theta - \frac{V_\theta^2}{r} = -\frac{1}{\rho} \frac{dp}{dr} + \nu \frac{\partial^2 V_r}{\partial z^2}, \quad (14)$$

$$z - \text{Momentum equation} \quad \frac{\partial}{\partial z} (p - \rho g_z z) = 0. \quad (15)$$

$$\text{Boundary conditions} \quad \text{at } r = r_i \quad \bar{V}_r = \bar{V}_{r,i}, \quad \bar{V}_\theta = \bar{V}_{\theta,i}, \quad (16)$$

$$\text{at } z = 0, b \quad V_r = 0, \quad V_\theta = 0, \quad (17)$$

$$\text{at } z = b/2 \quad \frac{\partial V_r}{\partial z} = \frac{\partial V_\theta}{\partial z} = 0. \quad (18)$$

There are three variables in Eqs. (12)–(18), which have not been described previously: kinematic viscosity of the working fluid ν , pressure p , and gravitational acceleration g .

Within the boundary layer developed on the flat solid discs, the relative tangential and radial velocities at any radius between r_o and r_i can be modelled as

$$V_\theta(r, z) = \bar{V}_{\theta,i} G_\theta(z) (\bar{V}_\theta(r) / \bar{V}_{\theta,i}) \quad (19)$$

$$V_r(r, z) = \bar{V}_{r,i} G_r(z) (\bar{V}_r(r) / \bar{V}_{r,i}), \quad (20)$$

where

$$R = \frac{r}{r_i}, G_\theta(z) = \frac{V_\theta(r, z)}{\bar{V}_\theta(r)} \text{ and } G_r(z) = \frac{V_r(r, z)}{\bar{V}_r(r)}. \quad (21)$$

The variable R in Eq. (21) represents the non-dimensional radius. The functions G_θ and G_r , which are respectively the z -variation of tangential and radial velocities within the boundary layers, are assumed to be parabolic in nature. The physical justification for the above assumptions is described in Ref. 13. The expressions of G_θ and G_r are given by

$$G_\theta = 6 \frac{z}{b} \left(1 - \frac{z}{b}\right), \quad (22)$$

$$G_r = 6 \frac{z}{b} \left(1 - \frac{z}{b}\right). \quad (23)$$

Equations (22) and (23) are applicable when the aspect ratio is small. When the aspect ratio is large, velocity profiles cease to be parabolic. The flow field can then be calculated by another analytical theory (currently under development) or by CFD simulations (as has been done in later example calculations given in this paper).

Integrating the differential form of the continuity equation (12), one obtains

$$\frac{\bar{V}_r(r)}{\bar{V}_{r,i}} = \frac{r_i}{r}. \quad (24)$$

We introduce the following three non-dimensional variables for further theoretical development:

$$p' = \frac{p - p_i}{\rho \Omega^2 r_i^2}, \quad \phi_i = \frac{\bar{V}_{r,i}}{\Omega r_i}, \quad \gamma = \frac{\bar{U}_{\theta,i}}{\Omega r_i}, \quad (25)$$

where p' is the non-dimensional pressure, ϕ_i is the flow coefficient, and γ is the tangential speed ratio at inlet. The θ -momentum equation (13) and r -momentum equation (14) are integrated partially with respect to z over the domain $(0, b/2)$. This makes it possible to transform the PDEs [Eqs. (13) and (14)] into ODEs. The complete analytical solutions of the ODEs are available in Ref. 13. The variation of V_θ along the radial direction is given by

$$\frac{\bar{V}_\theta(r)}{\bar{V}_{\theta,i}} = \frac{C_2}{C_1} + \left(1 - \frac{C_2}{C_1}\right) \frac{\exp\left[\frac{C_1}{2}(1 - R^2)\right]}{R}, \quad (26)$$

where

$$C_1 = \frac{10\nu}{\phi_i \Omega b^2}, \quad C_2 = \frac{-10}{6(\gamma - 1)}. \quad (27)$$

The analytical theory has been verified in Ref. 13 by comparing its predictions with experimental measurements available in the literature. A systematic dimensional analysis (providing the appropriate non-dimensional numbers for explaining and quantifying the flow physics of the rotating flow within the narrow spacing of multiple concentric discs), a similitude study (for achieving geometric, kinematic, and dynamic similarity between a model and the prototype), the proper scaling laws for obtaining Eqs. (12)–(15) from Navier-Stokes equations, and, the physical interpretation of C_1 and C_2 of Eq. (27) are given in Ref. 31. It is shown that $C_1 = 10/Ds$, where $Ds (\equiv \phi_i \Omega b^2 / \nu)$ is a new non-dimensional quantity introduced in Ref. 31 and the term ‘‘dynamic similarity number’’ has been coined to describe this variable. Seven non-dimensional numbers of importance have been identified for a Tesla disc turbine: (i) radius ratio ($\equiv r_o / r_i$), (ii) aspect ratio ($\equiv b / r_i$), (iii) tangential speed ratio

at inlet ($\equiv \bar{U}_{\theta,i} / \Omega r_i$), (iv) flow angle at inlet ($\equiv \tan^{-1} (|\bar{U}_{r,i}| / \bar{U}_{\theta,i})$) (which is same as the nozzle angle), (v) dynamic similarity number Ds , (vi) power coefficient ($\equiv \dot{W} / (\rho |\bar{U}_{r,i}|^3 r_i^2)$), and, (vii) pressure-drop coefficient ($\equiv (p_i - p_o) / (\rho \bar{U}_{\theta,i}^2)$). Geometric similarity is ensured by keeping the value of radius ratio and aspect ratio of the model same as that of the prototype. After achieving geometric similarity, dynamic similarity number, flow angle at inlet and tangential speed ratio at inlet of the model need to be equal with those of the prototype to ensure complete dynamic similarity between the model and the prototype. For a Tesla disc compressor (or pump), a similar analysis is applicable if two non-dimensional numbers are suitably modified: a flow coefficient ($\phi_i \equiv |\bar{U}_{r,i}| / \Omega r_i$) may be used instead of the flow angle at inlet, and, the non-dimensional number $\Omega b^2 / \nu$ may be used instead of the dynamic similarity number Ds .

B. Equivalence of Euler torque (Γ_{Euler}) and torque calculated from shear stress (Γ_{shear})

In this section, the equivalence between Γ_{shear} and Γ_{Euler} will be demonstrated from the mathematical theory described in Sec. III A. For this purpose, both sides of the θ -momentum equation (13) are multiplied by r and expressed as

$$r \frac{V_r}{r} \left[\frac{\partial}{\partial r} \{r (V_\theta + \Omega r)\} \right] = r \nu \frac{\partial^2 V_\theta}{\partial z^2}. \quad (28)$$

Using the relation between absolute and relative tangential velocity (Eq. (2)), Eq. (28) can be written in the following form:

$$V_r \left[\frac{\partial}{\partial r} (r U_\theta) \right] = r \nu \frac{\partial^2 V_\theta}{\partial z^2}. \quad (29)$$

Multiplying both sides of Eq. (29) by $\pi r \rho$ we get

$$\pi r \rho V_r \left[\frac{\partial}{\partial r} (r U_\theta) \right] = \pi r^2 \mu \frac{\partial}{\partial z} \left(\frac{\partial V_\theta}{\partial z} \right), \quad (30)$$

where, μ is the dynamic viscosity of the working fluid. Equation (30) is integrated partially with respect to z over the domain $(0, b/2)$ [using Eq. (18)],

$$\int_0^{b/2} \pi r \rho V_r \left[\frac{\partial}{\partial r} (r U_\theta) \right] \delta z = -\pi r^2 \tau_w(r), \quad (31)$$

where, $\tau_w = \tau_{z\theta}(z = 0, b)$ is the shear stress on the disc surface. Integrating Eq. (31) in the radial direction from outlet to inlet we get

$$\int_{r_o}^{r_i} \int_0^{b/2} \pi r \rho V_r \left[\frac{\partial}{\partial r} (r U_\theta) \right] \delta z \delta r = - \int_{r_o}^{r_i} \pi r^2 \tau_w(r) \delta r. \quad (32)$$

The order of integration is interchanged on the left-hand side of Eq. (32). The assumptions made in the analytical theory of Sec. III A mean that $\tau_{r\theta}(r = r_i)$ and $\tau_{r\theta}(r = r_o)$ can be neglected. Equation (10) then shows that for axi-symmetric flow,

$$\Gamma_{shear} = 4\pi \int_{r_i}^{r_o} r^2 \tau_w(r) dr. \quad (33)$$

Therefore, Eq. (32) can be rearranged as

$$\int_0^b \int_{r_o}^{r_i} 2\pi r \rho V_r \left[\frac{\partial}{\partial r} (r U_\theta) \right] \delta r \delta z = -\Gamma_{shear}. \quad (34)$$

Substituting the expression of V_r from Eqs. (20) and (24) into Eq. (34) we get

$$\int_0^b \int_{r_o}^{r_i} 2\pi \rho r_i \bar{V}_{r,i} G_r(z) \left[\frac{\partial}{\partial r} (r U_\theta) \right] \delta r \delta z = -\Gamma_{shear}. \quad (35)$$

Equation (35) can be simplified as

$$\int_0^b 2\pi \rho r_i \bar{V}_{r,i} G_r(z) (r_i U_{\theta,i} - r_o U_{\theta,o}) \delta z = -\Gamma_{shear}. \quad (36)$$

According to Eq. (21) $\bar{V}_{r,i} G_r(z) = V_{r,i}$, and according to Eq. (24) $V_{r,i}(r_i/r_o) = V_{r,o}$. Eq. (36) then becomes

$$2\pi \rho r_i^2 \int_0^b V_{r,i} U_{\theta,i} dz - 2\pi \rho r_o^2 \int_0^b V_{r,o} U_{\theta,o} dz = -\Gamma_{shear}. \quad (37)$$

Using Eqs. (4)–(7) and the condition of axi-symmetry, Eq. (37) can be expressed as

$$H_i - H_o = \dot{m} (r_i \hat{U}_{\theta,i} - r_o \hat{U}_{\theta,o}) = -\Gamma_{shear}. \quad (38)$$

Equations (9) and (38) show that

$$\Gamma_{Euler} = \Gamma_{shear}. \quad (39)$$

Equation (39) is the same as Eq. (11), the proposed work equivalence principle for the non-uniform viscous flow within a Tesla disc turbine. It is useful to summarize the route we took to demonstrate the validity of Eq. (39). We started with the differential θ -momentum equation (13), and used Eq. (20) and the solution of the continuity equation (24) to evaluate the LHS of Eq. (36). While deriving Eq. (39), it has not been necessary to actually evaluate $\partial V_\theta / \partial z$ using the analytical solution for V_θ (Eq. (19)) given in Sec. III A. It should be noted that Eq. (39) is valid only when Γ_{Euler} is calculated with the mass-flow-averaged absolute tangential velocities, $\hat{U}_{\theta,i}$ at inlet and $\hat{U}_{\theta,o}$ at outlet (not with area-averaged velocities, $\bar{U}_{\theta,i}$ and $\bar{U}_{\theta,o}$).

IV. INTERPRETATION OF TORQUE IN ABSOLUTE AND RELATIVE FRAMES: ROLE OF CORIOLIS FORCE

Γ_{Euler} , using the relation between absolute and relative velocities as described in Eq. (2), can be divided into two parts as given below

$$\Gamma_{Euler} = \dot{m} (\Omega r_o^2 - \Omega r_i^2) + \dot{m} (\hat{V}_{\theta,o} r_o - \hat{V}_{\theta,i} r_i). \quad (40)$$

It can be observed that both of the terms of Eq. (40) are proportional to mass flow rate. The term $\dot{m} (\Omega r_o^2 - \Omega r_i^2)$ depends on the rotational speed of the reference frame, whereas the term $\dot{m} (\hat{V}_{\theta,o} r_o - \hat{V}_{\theta,i} r_i)$ depends on the relative tangential velocity of the fluid. These two terms will be used multiple times in the subsequent theoretical discussion, henceforth these two terms are denoted as

$$(\Gamma_{Euler})_1 = \dot{m} \Omega (r_o^2 - r_i^2) \quad (41)$$

and,

$$(\Gamma_{Euler})_2 = \dot{m} (\hat{V}_{\theta,o} r_o - \hat{V}_{\theta,i} r_i). \quad (42)$$

It is recalled that, while demonstrating $\Gamma_{Euler} = \Gamma_{shear}$ in Sec. III B, it has not been necessary to actually evaluate $\partial V_\theta / \partial z$ using the analytical solution for V_θ (Eq. (19)) given in Sec. III A. We now want to evaluate $\partial V_\theta / \partial z$ using Eq. (19) to find out whether Γ_{shear} can be also naturally divided into two parts corresponding to the two components of Γ_{Euler} given by Eqs. (41) and (42).

First, the wall shear stress on one side of a single disc is calculated by using the definition of V_θ from Eq. (19). Therefore, the expression of wall shear stress is given by

$$\tau_w(r) = \left[\mu \frac{\partial V_\theta(r, z)}{\partial z} \right]_{at z=0} = \frac{6\mu \bar{V}_\theta(r)}{b}. \quad (43)$$

The expression of $\tau_w(r)$ from Eq. (43) is substituted in Eq. (33). Equation (33) is then integrated. This gives

$$\Gamma_{shear} = \frac{24\pi\mu\bar{V}_{\theta,i}r_i^3}{b} \left[\frac{C_2}{2C_1}(1-R_o^2) - \frac{\left(1-\frac{C_2}{C_1}\right)}{C_1} \left\{ 1 - \exp\left[\frac{C_1}{2}(1-R_o^2)\right] \right\} \right]. \quad (44)$$

where, R_o is the non-dimensional radius at outlet, i.e., $R_o \equiv r_o/r_i$.

The expression Γ_{shear} in Eq. (44) can be divided into two parts as given below

$$(\Gamma_{shear})_1 = \frac{24\pi\mu\bar{V}_{\theta,i}r_i^3}{b} \left[\frac{C_2}{2C_1}(1-R_o^2) \right] \quad (45)$$

and

$$(\Gamma_{shear})_2 = \left(\frac{24\pi\mu\bar{V}_{\theta,i}r_i^3}{b} \right) \left[-\frac{\left(1-\frac{C_2}{C_1}\right)}{C_1} \left\{ 1 - \exp\left[\frac{C_1}{2}(1-R_o^2)\right] \right\} \right]. \quad (46)$$

Equations (45) and (46) apparently suggest that both parts of the torque depend on the dynamic viscosity μ of the fluid; this seems logical from one's expectation from other fields of fluid dynamics. However, if the expressions of \dot{m} (from Eq. (3)) and C_1 (from Eq. (27)) are substituted in Eq. (45), then Eq. (45) becomes

$$(\Gamma_{shear})_1 = \frac{6}{5}\dot{m}\bar{V}_{\theta,i}r_i \left[\frac{C_2}{2}(1-R_o^2) \right]. \quad (47)$$

Equation (47) is a surprising result since it shows that part of the viscous torque, $(\Gamma_{shear})_1$, does not depend on the fluid viscosity at all. In order to understand what is then the source of this term, Eqs. (2), (25), and (27) are substituted in Eq. (47) to give

$$(\Gamma_{shear})_1 = \dot{m}\Omega(r_o^2 - r_i^2). \quad (48)$$

A comparison of Eqs. (41) and (48) shows that

$$(\Gamma_{shear})_1 = (\Gamma_{Euler})_1. \quad (49)$$

If the expressions of \dot{m} (from Eq. (3)) and C_1 (from Eq. (27)) are substituted in Eq. (46), then Eq. (46) becomes

$$(\Gamma_{shear})_2 = \left(-\frac{6}{5}\dot{m}\bar{V}_{\theta,i}r_i \right) \left(1 - \frac{C_2}{C_1} \right) \left[1 - \exp\left[\frac{C_1}{2}(1-R_o^2)\right] \right]. \quad (50)$$

For the axi-symmetric parabolic profiles, Eqs. (22) and (23), the definition of a mass-flow-averaged quantity (Eq. (5)) shows that the mass-flow-averaged and area-averaged velocities are related by

$$\hat{V}_\theta = \frac{6}{5}\bar{V}_\theta. \quad (51)$$

Substitution of $\bar{V}_\theta(R)/\bar{V}_{\theta,i}$ from Eq. (26), C_1 from Eqs. (27) and (51) into Eq. (50) gives

$$(\Gamma_{shear})_2 = \dot{m}(\hat{V}_{\theta,o}r_o - \hat{V}_{\theta,i}r_i). \quad (52)$$

A comparison of Eqs. (42) and (52) shows that

$$(\Gamma_{shear})_2 = (\Gamma_{Euler})_2. \quad (53)$$

A study of Eqs. (48) and (52) may suggest that, like $(\Gamma_{shear})_1$, $(\Gamma_{shear})_2$ is also independent of fluid viscosity. This is not however the case. Although μ does not appear explicitly in Eq. (52), its effect is implicitly present since, for a given $\hat{V}_{\theta,i}$, the value of $\hat{V}_{\theta,o}$ depends on the value of μ .

A. Work equivalence principle in the relative frame

In order to understand the physical origin of the component of “shear stress,” $(\Gamma_{shear})_1$ given by Eq. (48), we now attempt to derive the work equivalence principle in the rotating frame of reference. The proposed work transfer equation is encapsulated by the following qualitative statement:

$$\begin{array}{l} \text{Torque produced by the net} \\ \text{force acting on the fluid in the} \\ \text{control volume in the rotating} \\ \text{frame of reference} \end{array} = \begin{array}{l} \text{Change in angular} \\ \text{momentum of the} \\ \text{fluid in the rotating} \\ \text{frame of reference.} \end{array} \quad (54)$$

It is important to realize that *two* types of forces act on the fluid in the control volume, that have a moment about the axis of rotation i.e. the z -axis:

- (1) The shear force caused by the shear stress components, as explained in Sec. II B and Eq. (10).
- (2) The fictitious Coriolis force.

The torque produced by the shear force Γ_{shear} , discussed in Sec. II B, also applies to the rotating frame of reference since Eq. (2) shows that $\partial U_\theta / \partial z = \partial V_\theta / \partial z$. Let the torque produced by the fictitious Coriolis force is denoted by $\Gamma_{Coriolis}$ (whose magnitude is determined below). Equation (54) then can be written as

$$\boxed{\text{Work equivalence principle in the rotating frame of reference}} \quad \Gamma_{shear} + \Gamma_{Coriolis} = \dot{m} (\hat{V}_{\theta,o} r_o - \hat{V}_{\theta,i} r_i). \quad (55)$$

We now turn our attention to calculate $\Gamma_{Coriolis}$. Consider an annular ring of width dr and thickness dz at a radius r . The mass of fluid contained in this ring is $dm = \rho 2\pi r dr dz$. The magnitude of Coriolis acceleration of this mass of fluid in the θ -direction is $2\Omega |V_r|$. Thus the elemental torque produced by the Coriolis force on this elemental mass is $d\Gamma_{Coriolis} = r 2\Omega |V_r| dm = r 2\Omega |V_r| \rho 2\pi r dr dz$. Integrating the elemental Coriolis torque over all elemental annular rings in the control volume, one obtains

$$\Gamma_{Coriolis} = \int_{r_o}^{r_i} 2\Omega r \int_0^b |V_r| \rho 2\pi r dz dr. \quad (56)$$

The first integral is evaluated by Eq. (3). Equation (56) then becomes $\Gamma_{Coriolis} = \int_{r_o}^{r_i} 2\Omega \dot{m} r dr$. According to the continuity equation, \dot{m} remains constant at every circumferential plane at arbitrary r . \dot{m} is then independent of r and therefore can be taken outside the integral. Equation (56) therefore can be written as

$$\Gamma_{Coriolis} = \dot{m} \Omega (r_i^2 - r_o^2). \quad (57)$$

The expression of $\Gamma_{Coriolis}$ from Eq. (57) is substituted in Eq. (55) and is transposed to the RHS. The transposed equation (55) would then totally correspond to Eq. (40). This clearly identifies the origin of $(\Gamma_{shear})_1$ given by Eq. (48): $(\Gamma_{shear})_1 = (\Gamma_{Euler})_1 = -\Gamma_{Coriolis}$. It is important to recall that the complete expression for Γ_{shear} (Eq. (44)) was derived by integrating the expression of τ_w , which is given by Eq. (43) and is dependent on viscosity μ , over the disc surface area. The mystery of why a part of this viscous torque, $(\Gamma_{shear})_1$, would then be independent of viscosity is thus resolved once one takes the effect of Coriolis force in the rotating frame of reference (Eqs. (54), (55), and (57)).

V. COMPUTATIONAL FLUID DYNAMICS SOLUTION

A computational investigation of the fluid dynamics of work transfer within a Tesla disc turbine has been reported in this section. A commercially available CFD software CFX 14.5 is used to solve the full Navier-Stokes equation in the domain as defined in Sec. III A. CFX 14.5 is an element-based finite volume solver. Flow conservation equations are solved for finite volumes which are generated by discretizing the spatial domain into a mesh of discrete nodes. CFX 14.5 uses finite-element shape functions to evaluate the velocity and pressure at integration points from the velocity and pressure

at mesh nodes. CFX 14.5 uses co-located grid and therefore, special techniques proposed by Rhie and Chow³² and Majumdar³³ are implemented to avoid the formation of a decoupled (checkerboard) pressure field. The detailed procedure and solution methodology are given in Ref. 34. Various numerical schemes (upwind scheme, central difference scheme, high resolution scheme, etc.) are available in CFX 14.5 to evaluate the advection terms at the integration points. In the present study the high resolution scheme of CFX is used; the spatial order of the scheme may vary between one and two. Double precision arithmetic is adopted for all numerical calculations given in this paper.

The geometry of the model and the computational grid are generated by the commercially available software GAMBIT 2.4.6. The geometrical details (inlet radius, outlet radius, maximum inter-disc-spacing) and input flow variables ($\bar{U}_{\theta,i}$, $\bar{U}_{r,i}$) chosen for the present study are the same as those used in the experimental study in Ref. 10. Each disc has an inlet radius (r_i) of 25 mm [$R = 1$] and an outlet radius (r_o) of 13.2 mm [$R = 0.528$], and, the maximum inter-disc spacing considered is 0.46 mm. Computations have been carried out for many values of inter-disc spacing b (hence, for various values of aspect ratio \tilde{b}); however, only three representative computations corresponding to three selected values of \tilde{b} are reported in this section to highlight important observations and to keep the discussion focussed ($b = 0.46$ mm, $\tilde{b} = 0.0184$; $b = 0.23$ mm, $\tilde{b} = 0.0092$; and, $b = 0.115$ mm, $\tilde{b} = 0.0046$).

The flow is considered to be steady and laminar. The boundary conditions used in the present study are as follows:

1. The specified velocities at the inlet and static pressure at the outlet are assumed axi-symmetric.
2. At inlet, the area-averaged tangential velocity $\bar{U}_{\theta,i}$ is specified as 106 m/s and the area-averaged radial velocity $\bar{U}_{r,i}$ is -11.5 m/s. The chosen tangential and radial velocities imply a nozzle angle of 6.2° with the tangential direction. For computations reported in this section, it is assumed that there is no z -variation of the velocities. However, the effects of non-uniformity of inlet velocities in the z -direction have been studied in Sec. VI (with the same values of $\bar{U}_{\theta,i}$ and $\bar{U}_{r,i}$ mentioned above).
3. At outlet, the boundary condition is modelled as pressure outlet with zero gauge pressure.
4. No slip boundary condition is set on the disc walls. A rotational speed (Ω) of the disc (wall) is also set.

Numerical simulations are carried out for a large number of γ (by varying Ω of the disc), and out of these many calculations, the results for three particular values of γ are discussed in this paper ($\Omega = 1000$ rad/s, $\gamma = 4.24$; $\Omega = 3000$ rad/s, $\gamma = 1.413$; $\Omega = 5000$ rad/s, $\gamma = 0.848$). The quantitative solutions given in this paper are valid for a particular fluid, viz., air.

In order to systematically select an appropriate convergence criterion, the flow for the same computational domain has been simulated thrice as the maximum residual is set respectively at 10^{-5} , 10^{-6} , and 10^{-7} . It is found that when the maximum residual is changed from 10^{-6} to 10^{-7} , the corresponding changes in both area-averaged and mass-flow-averaged radial and tangential velocities are less than 0.05%. Hence, a maximum residual of 10^{-6} is chosen as the convergence criterion for the present study.

A grid-independence test has been carried out (Table I showing a few pertinent details), and based on this study, a total of 2 280 000 ($120 \times 190 \times 100$) mapped, hexahedral computational cells are used for the results presented in this paper. The grids are distributed differently in the r , θ , and z directions in accordance with the difference in the flow physics in the three directions. The grid

TABLE I. Grid independence test for $r_i = 25$ mm ($R = 1$), $r_o = 13.2$ mm ($R = 0.528$), $b = 0.46$ mm ($\tilde{b} = 0.0184$), $\Omega = 3000$ rad/s ($\gamma = 1.413$).

| Grid Distribution | Number of grids in r , θ , and z directions | Total number of grids | Δp_{i_o} (Pa) |
|-------------------|--------------------------------------------------------|-----------------------|-----------------------|
| Coarse | (60 × 95 × 50) | 285 000 | 13 165.3 |
| Standard | (120 × 190 × 100) | 2 280 000 | 13 233.6 |
| Fine | (168 × 266 × 140) | 6 256 320 | 13 235 |

distribution in the z -direction is non-uniform with very small grid size close to the surfaces of the two discs (to capture the velocity gradient on the surface accurately) and with progressively larger grid size as one moves away from the surfaces to the middle of the inter-disc gap (with a successive ratio of 1.05). Since the applied boundary conditions are axi-symmetric, the grids in the θ -direction are uniformly distributed. In course of the present study, it has been found that, when there is no z -dependence in the applied boundary conditions at inlet for the radial and tangential velocities, both velocities change very rapidly within a very short radial distance from the inlet, within which the z -profile of both velocities are created from their uniform values at inlet. In order to capture this effect properly, the grids in the radial direction are divided into two zones—non-uniform and uniform. Near the inlet, non-uniform boundary-layer-type grids with 20 rows in the radial direction are used. The size of the first grid is 0.003 mm and the successive ratio of the geometric progression series is 1.2. The rest of the radial extent up to the outlet is meshed uniformly with 100 grid points. The rapid attainment of the z -dependence of the absolute tangential velocity within a short radial distance of the inlet is shown in Figure 4.

Instead of performing a detailed grid independence test for every value of inter-disc spacing b studied in the present paper, we have performed the grid independence study only for the maximum value of b as shown in Table I and have used the same grid ($120 \times 190 \times 100$), described above, for all other values of b (which are lower than $b = 0.46$ mm). As the value of b decreases, the same accuracy could be obtained with correspondingly reduced number of grids in the z -direction, but the finer grid did not pose a severe constraint on the computational resources available to us.

The mass-flow-averaged and the area-averaged velocities are computed at the inlet and the outlet. Γ_{Euler} is then obtained from Eq. (9) on the basis of the mass-flow-averaged velocities. Detailed computations reveal that there are subtle differences in the mechanism of work transfer as the aspect ratio (\tilde{b}) is altered or the tangential speed ratio (γ) is varied.

Table II shows the results of the numerical simulation for three different aspect ratios (\tilde{b}) corresponding to three inter-disc-spacings (b). For each of \tilde{b} the results are presented for two values of γ . Mass-flow-averaged (\hat{U}_θ) and area-averaged tangential velocities (\bar{U}_θ) are calculated at the inlet and the outlet. It can be observed from Table II that \hat{U}_θ and \bar{U}_θ are in general not equal. Euler torque (Γ_{Euler}) is calculated on the basis of \hat{U}_θ . The area-averaged formulation [$\dot{m}(\bar{U}_{\theta,o}r_o - \bar{U}_{\theta,i}r_i)$] is performed on the basis of \bar{U}_θ . Γ_{shear} is obtained from the numerical simulations. While comparing the values it can be seen that Γ_{shear} and Γ_{Euler} are almost equal in all the cases considered here. In accordance with the analytical demonstrations contained in Sec. III, the CFD results also establish the equality of Γ_{shear} and Γ_{Euler} provided the mass-flow-averaged tangential velocities are used as in Eq. (9).

Table II shows that for smaller aspect ratios (0.0046, 0.0092) the torque calculated by using area-averaged tangential velocities is greater than the torque calculated by using mass-flow-averaged

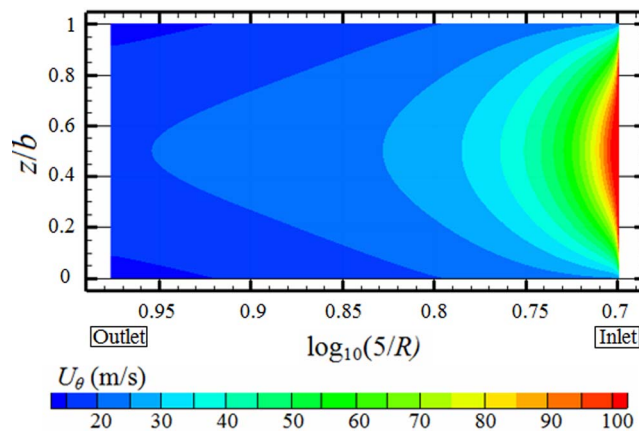


FIG. 4. Contour of the absolute tangential velocity (U_θ) on a rz plane. [$r_i = 25$ mm ($R = 1$, $\log_{10}(5/R) = 0.699$), $r_o = 13.2$ mm ($R = 0.528$, $\log_{10}(5/R) = 0.976$), $b = 0.115$ mm ($\tilde{b} = 0.0046$), $\phi_i = -0.46$, $\gamma = 4.24$, and air is used as working fluid. The specially stretched x -axis is chosen so that the flow details near the inlet are clearly visible.]

TABLE II. Comparison of Euler torque (Γ_{Euler}), torque calculated by area-averaged formulation ($\dot{m}(\bar{U}_{\theta,o}r_o - \bar{U}_{\theta,i}r_i)$) and torque due to shear stress (Γ_{shear}) computed from CFD simulation (For all calculations $r_i = 25$ mm ($R = 1$), $r_o = 13.2$ mm ($R = 0.528$), and air is used as working fluid. For uniform velocity profile at inlet $\hat{U}_{\theta,i} = \bar{U}_{\theta,i} = 106$ m/s.)

| \tilde{b} | γ | ϕ_i | $\hat{U}_{\theta,o}$ (m/s) | $\bar{U}_{\theta,o}$ (m/s) | $\Gamma_{Euler} = \dot{m}$ ($\hat{U}_{\theta,o}r_o - \hat{U}_{\theta,i}r_i$) (N m) | Area-averaged | | Power output from a disc-pair (W) |
|-------------|----------|----------|-------------------------------|-------------------------------|--------------------------------------------------------------------------------------------|---------------|---------------------------|-----------------------------------------|
| | | | | | | formulation | Γ_{shear} (N m) | |
| 0.0184 | 4.24 | -0.46 | 87.832 | 100.695 | -0.001467 | -0.001299 | -0.001471 | 1.47 |
| 0.0184 | 1.413 | -0.153 | 121.201 | 136.297 | -0.001034 | -0.000837 | -0.001035 | 3.11 |
| 0.0092 | 4.24 | -0.46 | 45.478 | 41.095 | -0.001009 | -0.001034 | -0.001016 | 1.02 |
| 0.0092 | 1.413 | -0.153 | 85.717 | 82.098 | -0.000750 | -0.000770 | -0.000750 | 2.25 |
| 0.0046 | 4.24 | -0.46 | 17.659 | 16.890 | -0.000590 | -0.000590 | -0.000600 | 0.60 |
| 0.0046 | 1.413 | -0.153 | 52.795 | 50.567 | -0.000480 | -0.000490 | -0.000480 | 1.44 |

tangential velocities. This trend is opposite to that which is observed for comparatively larger aspect ratio (0.0184). The reason for this can be explained as follows.

For small aspect ratio, the radial and tangential velocity components starting with a uniform distribution (both in the θ and z -directions) at inlet become parabolic (in the z -direction) within a short radial distance. Equation (51) shows that the mass-flow-averaged tangential velocity is greater than the area-averaged tangential velocity. Therefore, the magnitude of $\hat{U}_{\theta,o}$ is greater than $\bar{U}_{\theta,o}$ due to the parabolic distribution. However, $\hat{U}_{\theta,i} = \bar{U}_{\theta,i}$ because of the uniform velocity distribution at inlet. This makes the magnitude of the term ($U_{\theta,o}r_o - U_{\theta,i}r_i$) in Eq. (1) greater while the Euler torque is calculated using the area-averaged tangential velocities for smaller aspect ratio. When the aspect ratio is large (e.g., 0.0184), the z -distribution of the radial velocity V_r is not parabolic but is more complex with low values in the central region (where the tangential velocity U_θ component is large). This makes the mass-flow-averaged $\hat{U}_{\theta,o}$ less than the area-averaged $\bar{U}_{\theta,o}$.

Guha and Sengupta¹⁴ had shown that the variations of the area-averaged relative tangential velocity within a Tesla disc turbine depend on the local balance of various forces. The θ -momentum equation (13) may be interpreted as a relation that specifies the value of $\frac{\partial V_\theta}{\partial r}$, i.e., how V_θ changes with r . In Eq. (13), $2\Omega V_r$ is the θ -component of Coriolis acceleration, the term $(V_r V_\theta)/r$ takes an important part to conserve the angular momentum of the working fluid, the term $\nu \frac{\partial^2 V_\theta}{\partial z^2}$ represents the viscous (frictional) acceleration (a negative value would show that it is in fact a deceleration). Depending on the relative magnitudes of these accelerations, $\frac{\partial V_\theta}{\partial r}$ may be positive, zero or negative.

For $\gamma > 1$, V_θ increases for the combined effect of $\frac{V_r V_\theta}{r}$ and $2\Omega V_r$, while it decreases due to the effect of $\nu \frac{\partial^2 V_\theta}{\partial z^2}$.¹⁴ As one moves from the inlet to the outlet, the effect of $\nu \frac{\partial^2 V_\theta}{\partial z^2}$ may dominate at first, then the combined effect of $(V_r V_\theta)/r$ and $2\Omega V_r$ overtakes. With decreasing r , V_θ then decreases to a minimum at a certain radius (whose value depends on \tilde{b} and γ , and would be observable only if the value of this radius is greater than the outlet radius used in the particular design) and then onwards increases. For certain geometry and flow conditions (for example at high Ω), V_θ may become quite large at the outlet. Equation (2) shows that U_θ depends on V_θ and Ωr . Although, Ωr decreases as one moves from the inlet to the outlet, U_θ may sometimes increase since V_θ increases. This is the reason why in Table II one finds that the absolute tangential velocity at outlet is greater than that at inlet when $\tilde{b} = 0.0184$ and $\gamma = 1.413$ (which corresponds to large Ω).

The magnitude of the viscous term $\nu \frac{\partial^2 V_\theta}{\partial z^2}$ increases with an increase in γ and with a decrease in \tilde{b} . For large γ and small \tilde{b} , V_θ may therefore decrease rapidly and substantially as one moves radially from the inlet to the outlet, so much so that even after the subsequent increase due to the combined effect of $(V_r V_\theta)/r$ and $2\Omega V_r$ the magnitude of V_θ at the outlet remains low. This is why in

TABLE III. Mass-flow-averaged and area-averaged relative tangential velocities at inlet and outlet (For all calculations $r_i = 25$ mm ($R = 1$), $r_o = 13.2$ mm ($R = 0.528$), and air is used as working fluid.)

| \tilde{b} | γ | ϕ_i | $\hat{V}_{\theta,i} = \bar{V}_{\theta,i}^a$ (m/s) | $\hat{V}_{\theta,o}$ (m/s) | $\bar{V}_{\theta,o}$ (m/s) |
|-------------|----------|----------|---------------------------------------------------|----------------------------|----------------------------|
| 0.0184 | 4.24 | -0.46 | 81 | 74.632 | 87.495 |
| 0.0184 | 1.413 | -0.153 | 31 | 81.601 | 96.697 |
| 0.0092 | 4.24 | -0.46 | 81 | 32.278 | 27.895 |
| 0.0092 | 1.413 | -0.153 | 31 | 46.117 | 42.498 |
| 0.0046 | 4.24 | -0.46 | 81 | 4.459 | 3.690 |
| 0.0046 | 1.413 | -0.153 | 31 | 13.195 | 10.967 |

^aThe equality is true only because a uniform velocity profile is assumed at inlet for these example calculations.

Table III the value of V_θ at outlet is substantially smaller than that at inlet when $\gamma = 4.24$ and $\tilde{b} = 0.0046$ or $\tilde{b} = 0.0092$. For these cases, the value U_θ at outlet is also substantially smaller than that at inlet (see Table II). However, in order to find out whether this trend in the variation of V_θ and U_θ continues if the outlet radius is progressively reduced, a series of further computations with outlet radius smaller than that of the experimental Tesla turbine (for whose dimensions the computational results are reported in this paper) were undertaken. A selected case ($r_o/r_i = 0.2$, $\tilde{b} = 0.006$, $\gamma = 1.413$) from these computations is depicted in Figure 5. Figures 5(a) and 5(b) show that, for $\gamma > 1$, though V_θ and U_θ initially decreases as one moves radially inward from the inlet, both quantities eventually increase (this changeover may take place quite close to the axis of rotation if the inter-disc spacing is very small). Figure 5(c) further shows that the absolute value of radial velocity $|U_r|$ progressively increases in the negative r -direction i.e., towards the outlet. It is so because the flow area ($2\pi rb$) decreases with a decrease in r and the fluid flow (steady, incompressible, and axi-symmetric) has to satisfy the equation of continuity.

The distribution of absolute tangential velocity (U_θ) in the flow domain is discussed above. Equation (1) shows that Γ_{Euler} depends on the product of absolute tangential velocity and radius (i.e., $U_\theta r$). The term $\Omega(U_{\theta,o}r_o - U_{\theta,i}r_i)$ signifies the change in specific enthalpy from inlet to outlet within a Tesla disc turbine. Under steady state condition for a particular Ω , the parameter $U_\theta r$ is determined by post-processing the CFD results. Iso-surfaces of $U_\theta r$ are computed to find out the spatial distribution of specific work transfer in the narrow gap between two consecutive discs. Figures 6 and 7 reveal the detailed fluid dynamics of the work transfer, depicting two qualitatively different spatial distributions of $U_\theta r$ for fluid flow with two different values of aspect ratio.

Figure 6 represents the iso-surfaces of $U_\theta r$ for very small aspect ratio (i.e., 0.0046). Figure 7 represents the iso-surfaces of $U_\theta r$ for a comparatively larger aspect ratio (i.e., 0.0184). The tangential speed ratio γ for both cases is set as 4.24. The tangential and radial velocities at inlet are the same as discussed previously. Figures 6(a), 6(b), and 7(a) appear shorter in the z -direction as compared to the rest of the figures. They represent iso-surfaces close to the outlet; hence the orientation of the three-dimensional isometric views creates the impression of shorter height.

Figures 6(e) and 7(f) show that $U_\theta r$ is uniform at inlet because the uniform boundary condition for U_θ is specified there. As the working fluid moves spirally inward, the flow becomes non-uniform (see Figures 6(a)–6(d) and 7(a)–7(e)). The nature of non-uniformity can be assessed by observing the bends of the iso-surfaces of $U_\theta r$. The shapes of the surfaces signify that the value of $U_\theta r$ is relatively small near the surfaces of the discs. This occurs because of the effect of boundary layers which develop over the surfaces of the discs where no-slip boundary conditions in the relative frame are specified. A comparison of Figures 6 and 7 shows that the drop of specific enthalpy in the radial direction is more gradual for larger \tilde{b} . Figure 6 shows that for smaller \tilde{b} (and $\gamma = 4.24$), most of the drop in specific enthalpy occurs near the inlet. It can be seen from Figure 6(b) that near the outlet $U_\theta r$ is more or less uniform throughout the disc spacing (whereas Figures 7(a) and 7(b) show that low values of $U_\theta r$ are located near the surface of the disc). This feature can be verified from the results presented in Table II. On the other hand, Figure 7 shows that, for larger \tilde{b} , non-uniformity exists in the whole flow domain except at the inlet (for the specified boundary condition). Hence mass-flow-averaging is a must to calculate the Euler work for a Tesla turbine with comparatively

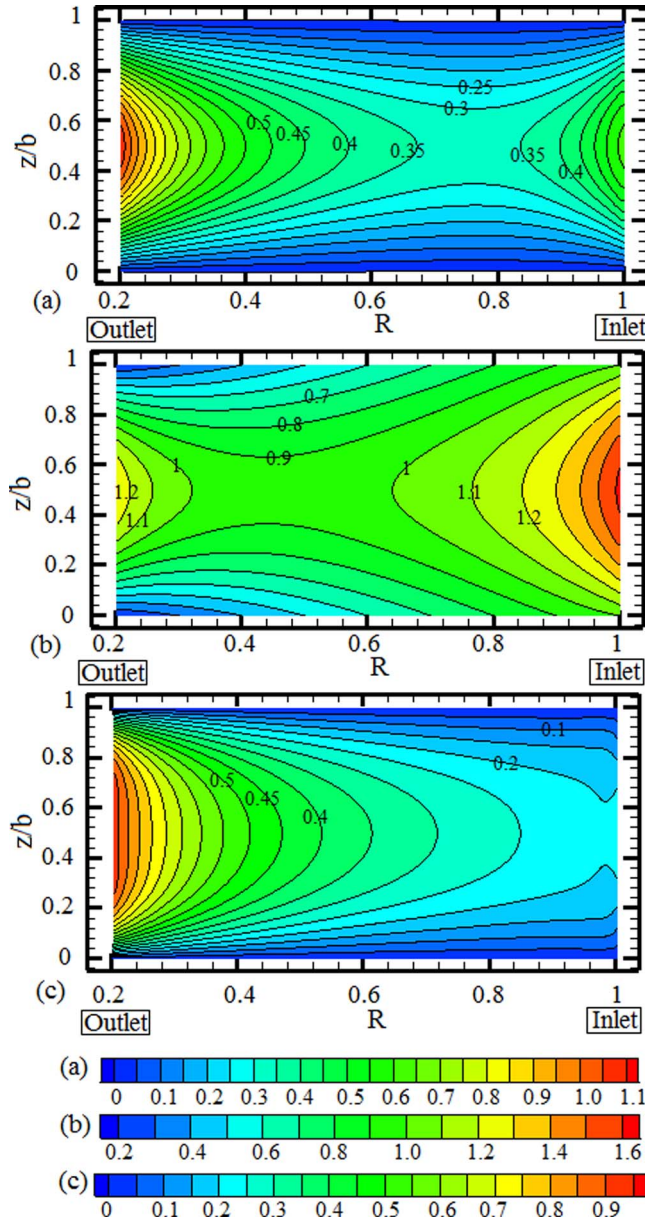


FIG. 5. Contour of non-dimensional velocities on a rz plane. (a) Contour of $V_\theta/(\Omega r_i)$; (b) contour of $U_\theta/(\Omega r_i)$; (c) contour of $|U_r|/(\Omega r_i)$; Results obtained from CFD simulation for $R_o = 0.2$, $\tilde{b} = 0.006$, $\gamma = 1.413$, $\phi_i = -0.153$, parabolic velocity distribution at inlet and air as working fluid are used.

larger \tilde{b} . Table II also shows that the disparity between the Euler torque (Γ_{Euler}) and torque calculated by area-averaged formulation ($\dot{m}(\tilde{U}_{\theta,o}r_o - \tilde{U}_{\theta,i}r_i)$) is greater in the case of larger \tilde{b} . Figures 6 and 7 signify the fact that more work within a shorter radial span can be extracted from the fluid stream if one uses smaller \tilde{b} .

Figure 8 shows a case of flow reversal¹⁴ which occurs in the relative frame of reference when $\gamma < 1$. The computation has been carried out for $\tilde{b} = 0.0184$. The inner and outer radius of the discs and the boundary conditions at inlet and outlet planes remain the same as mentioned above. The rotational speed of the discs are set to 5000 rad/s for which $\gamma = 0.848$. Plane 2 of Figure 8 shows the contour of $V_\theta/(\Omega r_i)$ on a rz plane (as the flow is axi-symmetric V_θ does not vary in the θ -direction) which is extended from $r = r_i$ to $r = r_o$ and from $z = 0$ to $z = b$. It can be seen that $V_\theta/(\Omega r_i)$ is negative at inlet (except on the surfaces of the discs where $V_\theta = 0$) and positive at outlet.

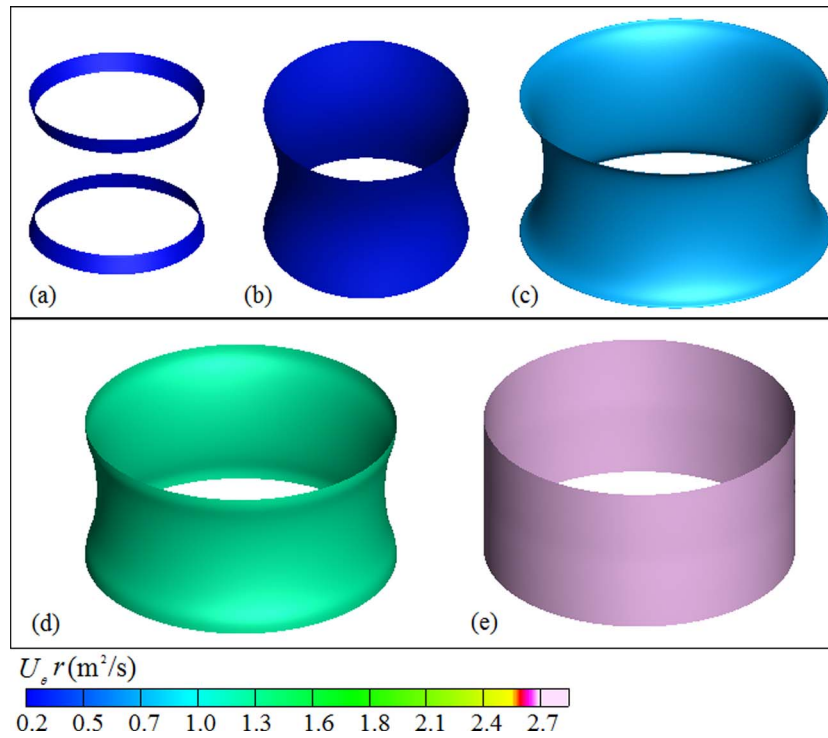


FIG. 6. (a)–(e) Spatial distribution of $U_\theta r$ within a Tesla disc turbine for small inter-disc spacing. [$r_i = 25$ mm ($R = 1$), $r_o = 13.2$ mm ($R = 0.528$), $\bar{b} = 0.0046$, $\gamma = 4.24$, $\phi_i = -0.46$, and air is used as working fluid.]

Hence, V_θ is negative at inlet but positive at outlet. Somewhere between the inlet and the outlet, the flow reversal in the relative frame of reference has taken place. This is indicated by the dotted line on Plane 2 in Figure 8.

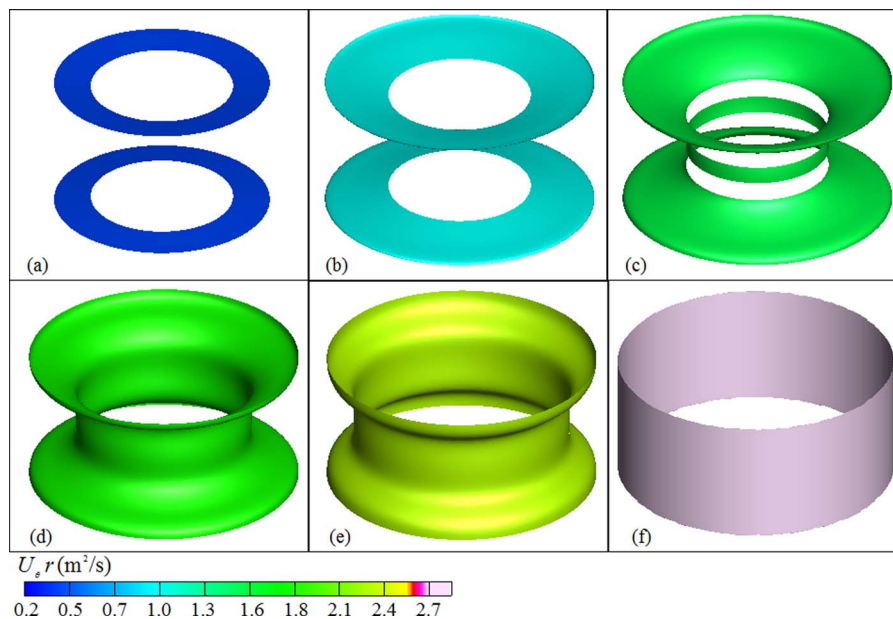


FIG. 7. (a)–(f) Spatial distribution of $U_\theta r$ within a Tesla disc turbine for large inter-disc spacing. [$r_i = 25$ mm ($R = 1$), $r_o = 13.2$ mm ($R = 0.528$), $\bar{b} = 0.0184$, $\gamma = 4.24$, $\phi_i = -0.46$, and air is used as working fluid.]

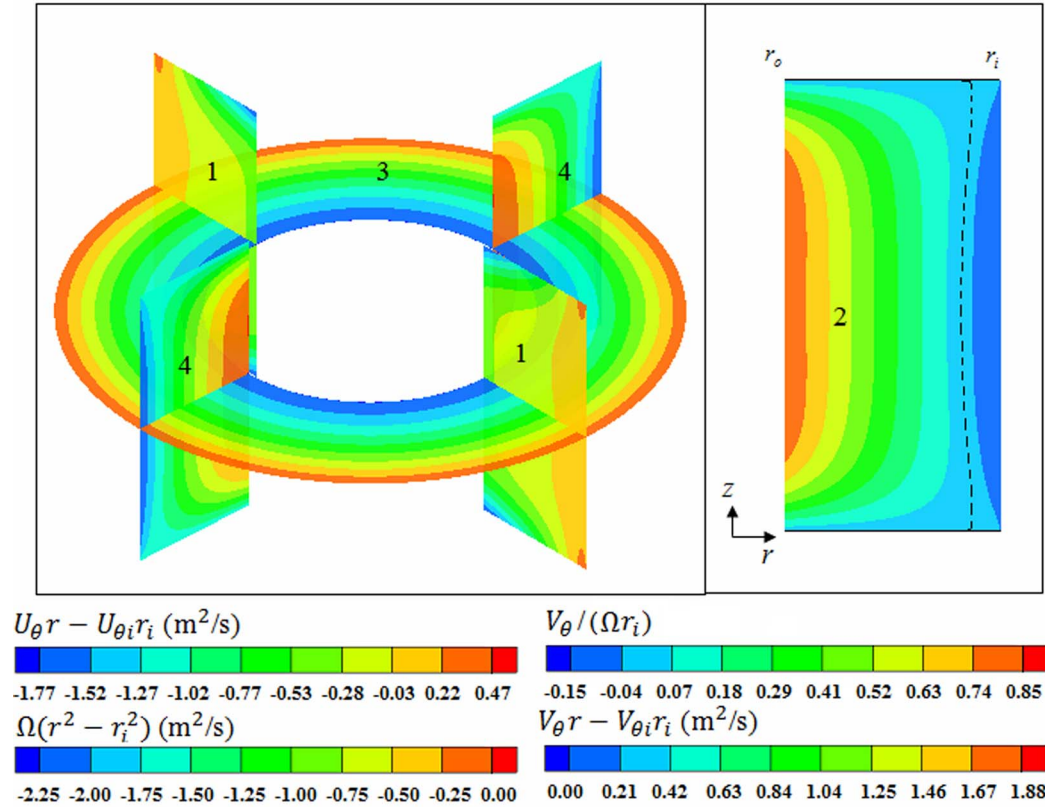


FIG. 8. Distribution of $U_{\theta}r - U_{\theta,i}r_i$ and its two components (derived from Eq. (2)) in the computational domain for $\gamma < 1$ (a case of flow reversal in the relative frame reference). [$r_i = 25$ mm ($R = 1$), $r_o = 13.2$ mm ($R = 0.528$), $\tilde{b} = 0.0184$, $\gamma = 0.848$, $\phi_i = -0.092$, and air is used as working fluid. Plane 1: $U_{\theta}r - U_{\theta,i}r_i$, Plane 2: $V_{\theta}/(\Omega r_i)$, Plane 3: $\Omega(r^2 - r_i^2)$, Plane 4: $V_{\theta}r - V_{\theta,i}r_i$. Flow reversal occurs across the dotted line shown in Plane 2.]

Plane 1, Plane 3, and Plane 4 show the contours of $U_{\theta}r - U_{\theta,i}r_i$, $\Omega(r^2 - r_i^2)$ and $V_{\theta}r - V_{\theta,i}r_i$, respectively when $\gamma < 1$ (a case of flow reversal in the relative frame reference). It can be observed from the contours on Plane 1 that, starting from zero at inlet, the value of $U_{\theta}r - U_{\theta,i}r_i$ is positive near the inlet. This signifies the fact that up to some radial position, the fluid absorbs power from the surfaces of the discs. When the working fluid moves further downstream, the value of $U_{\theta}r - U_{\theta,i}r_i$ becomes negative. Hence, considering the total extent of disc-surfaces, net power is transmitted from the fluid to the discs, and the turbine can generate shaft power output. Now, using Eq. (2) one may divide $U_{\theta}r - U_{\theta,i}r_i$ into two parts: $\Omega(r^2 - r_i^2)$ and $V_{\theta}r - V_{\theta,i}r_i$. It can be seen from Plane 4 that $V_{\theta}r - V_{\theta,i}r_i$ is always positive. This shows that the control volume can only absorb power from the surfaces of the two discs for $(\Gamma_{Euler})_2$. However, Plane 3 shows that the term $\Omega(r^2 - r_i^2)$ is always negative. Thus, $(\Gamma_{Euler})_1$, the torque produced by the Coriolis force, is such that, even for the flow reversal case when the value of γ is above a certain limiting value (see Eq. (60) given later), the Tesla disc turbine is able to produce net shaft power output.

Figures 9 and 10 show how the angular momentum transfer from the fluid to the surfaces of the discs depends on the values of aspect ratio (\tilde{b}) and tangential speed ratio (γ), while the fluid moves from inlet ($R = 1$) to outlet ($R = 0.528$). Both of the figures show the results obtained from CFD simulations performed for three values of \tilde{b} . Figure 9 represents the calculations for $\gamma = 4.24$ and Figure 10 represents the calculations for $\gamma = 1.413$. If H_i is the angular momentum at the inlet circumferential plane and H is the angular momentum at any arbitrary circumferential plane between the inlet and outlet, $H_i - H$ will be the drop of angular momentum of the fluid starting from inlet up to that plane. At this point, a new non-dimensional quantity called the torque

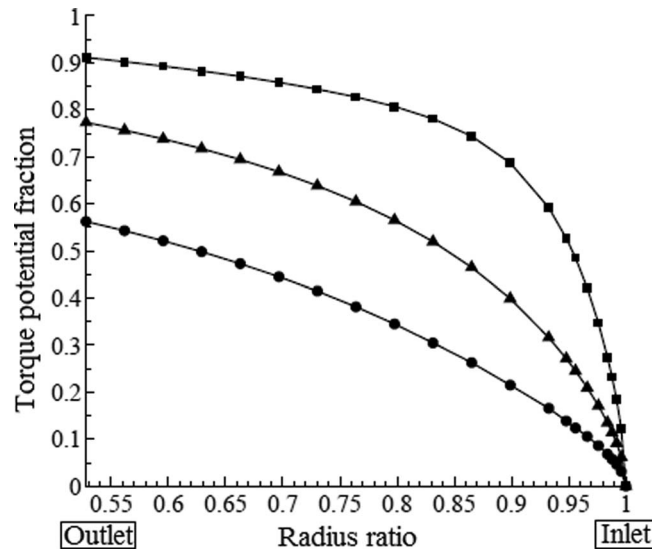


FIG. 9. The drop of angular momentum in the radial direction for various aspect ratios at $\gamma = 4.24$. [$r_i = 25$ mm ($R = 1$), $r_o = 13.2$ mm ($R = 0.528$), $\gamma = 4.24$, $\phi_i = -0.46$, and air is used as working fluid. Keys: \bullet $\tilde{b} = 0.0184$, \blacktriangle $\tilde{b} = 0.0092$, \blacksquare $\tilde{b} = 0.0046$.]

potential fraction $\Delta\tilde{H}$, where $\Delta\tilde{H} \equiv (H_i - H)/H_i$, is introduced. In this interpretation the value of H_i is viewed as the maximum torque potential available at the inlet of the disc turbine and the value of $\Delta\tilde{H}$ at the outlet indicates what fraction of this inlet torque potential is actually realized at the particular operating condition. In comparison to Tables II and III which gives the data only at the inlet and outlet planes, Figures 9 and 10 show the local variation of H from the inlet to the outlet.

The following general observations can be made from Figures 9 and 10:

The value of $\Delta\tilde{H}$ at any radial position increases with a decrease in the value of \tilde{b} . This signifies that, for smaller values of \tilde{b} , a greater fraction of H_i can be extracted between the two rotating discs.

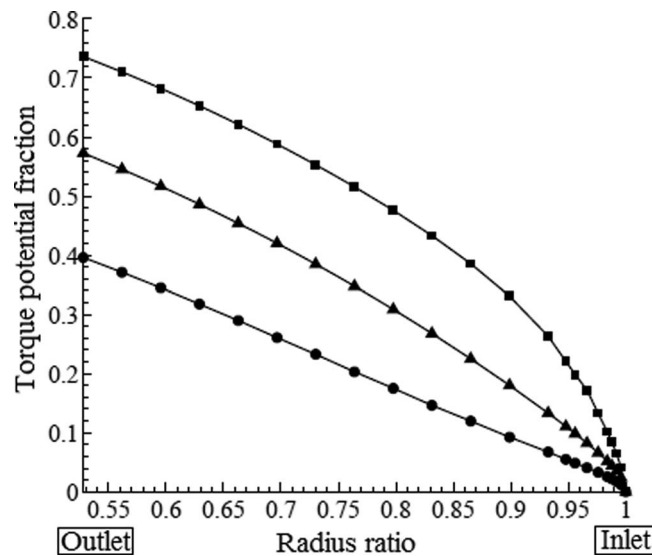


FIG. 10. The drop of angular momentum in the radial direction for various aspect ratios at $\gamma = 1.413$. [$r_i = 25$ mm ($R = 1$), $r_o = 13.2$ mm ($R = 0.528$), $\gamma = 1.413$, $\phi_i = -0.153$ and air is used as working fluid. Keys: \bullet $\tilde{b} = 0.0184$, \blacktriangle $\tilde{b} = 0.0092$, \blacksquare $\tilde{b} = 0.0046$.]

Secondly, it can be observed from Figures 9 and 10 that for small value of aspect ratio ($\tilde{b} = 0.0046$) and large value of tangential speed ratio ($\gamma = 4.24$), most of the angular momentum is transferred from the fluid to the surfaces of the discs in the inlet region. To comprehend this issue, Eq. (40) is expressed in the following form:

$$H_i - H = \dot{m} (\Omega r_i^2 - \Omega r^2) + \dot{m} (\hat{V}_{\theta,i} r_i - \hat{V}_{\theta} r). \quad (58)$$

The term $\dot{m} (\Omega r_i^2 - \Omega r^2)$ in Eq. (58) is a simple quadratic function of radius and this dependence is universal for all values of r and b . The term $\dot{m} (\hat{V}_{\theta,i} r_i - \hat{V}_{\theta} r)$, on the other hand, is a complex function of r and b because the local value of the relative tangential velocity \hat{V}_{θ} depends in a complex fashion on r and b (and several other factors such as the viscosity of the fluid). When \tilde{b} is small, the frictional force is large (particularly so for low values of Ω which indicates high relative velocity between the disc and fluid since the inlet absolute tangential velocity is held constant in the analysis) and the relative tangential velocity decreases substantially within a short radial distance from the inlet plane. Therefore, the value of $\Delta \tilde{H}$ also changes rapidly within a short radial distance from the inlet. Keeping \tilde{b} fixed at a small value, if γ is increased (i.e., Ω is decreased) then the change in $\Delta \tilde{H}$ becomes greater in the inlet region but $\Delta \tilde{H}$ increases at a lower rate near the outlet. This behaviour can be seen if Figures 9 and 10 are compared with each other.

Thirdly, it is found that, when the value of \tilde{b} is large (say 0.0184), the rapid change of $\Delta \tilde{H}$ in the inlet region does not take place. The change in angular momentum in the radial direction is more uniformly distributed between the inlet and outlet.

VI. EXACT THEORY VERSUS AREA-AVERAGING APPROACH

In turbomachinery calculations, the area-averaged quantities are sometimes used (e.g., Ref. 35). Area-averaged quantities have also been used for the calculation of performance of Tesla disc turbines (e.g., Ref. 36). The advantage of the area-averaging approach is the simplicity of the formulation. It may be useful in engineering solutions of overall parameters when details are not known.

The analysis of Sec. II A shows how the presence of flow non-uniformity can be reflected in the calculation of flow rate of angular momentum through any circumferential surface $\left(H = r^2 \int_0^b \int_0^{2\pi} \rho U_{\theta} |V_r| d\theta dz \right)$, and, in particular, how the simultaneous z -variation of two mutually perpendicular velocity components U_{θ} and V_r can be accommodated in a consistent theoretical formulation. The mathematical analysis shows how the mass-flow-averaged tangential velocities arise naturally in Eqs. (6) and (7), and should be the adopted methodology for accurately analyzing the flow through Tesla disc turbomachines. Accurate accounting is required in the enunciation of a scientific principle such as the equality of Γ_{Euler} (determined from the change in angular momentum) and Γ_{shear} (determined from the integrated effect of the shear stress acting on the disc surface), as encapsulated by Eq. (11).

Although the terminology “mass-flow-averaged” is used in the present paper to evoke familiarity with a concept used in conventional turbomachine, the application of the concept in the present work is subtly unique. Conventionally, the mass-flow-average of a scalar quantity is used (e.g., mass-flow-averaged enthalpy, mass-flow-averaged entropy, mass-flow-averaged total pressure, etc.). In the present work, mass-flow-average of a velocity component, which is at right angle to the velocity component that determines the mass flow rate, is involved. Both velocity components are non-uniform: they are certainly strongly non-uniform in the z -direction, there can also be non-uniformity in the θ -direction.

A study of Table II shows that for certain geometries and flow conditions, the difference between the mass-flow-averaging and area-averaging approaches may be small in determining the overall torque, though very large differences are also possible. It may not be possible to predict how large the difference would be, *a priori*, without performing both calculations

TABLE IV. Comparison of Euler torque (Γ_{Euler}), torque calculated by area-averaged formulation ($\dot{m}(\bar{U}_{\theta,o}r_o - \bar{U}_{\theta,i}r_i)$) and torque due to shear stress (Γ_{shear}) computed from CFD simulation for non-uniform inlet velocity profile (parabolic in the z-direction: Eqs. (22) and (23)). (For all calculations $r_i = 25$ mm ($R = 1$), $r_o = 13.2$ mm ($R = 0.528$), $\gamma = 4.24$, $\phi_i = -0.46$, $\bar{U}_{\theta,i} = 122.196$ m/s, $\bar{U}_{\theta,o} = 106$ m/s, and air is used as working fluid.)

| \bar{b} | $\hat{U}_{\theta,o}$ (m/s) | $\bar{U}_{\theta,o}$ (m/s) | $\Gamma_{Euler} =$ $\dot{m}(\bar{U}_{\theta,o}r_o - \bar{U}_{\theta,i}r_i)$ (N m) | Area-averaged | Γ_{shear} (N m) | $\Delta\bar{H}_o$ | Power output from a disc-pair (W) |
|-----------|-------------------------------|-------------------------------|-----------------------------------------------------------------------------------------|----------------------------------------------------------------------------------|---------------------------|-------------------|-----------------------------------------|
| | | | | formulation $\dot{m}(\bar{U}_{\theta,o}r_o - \bar{U}_{\theta,i}r_i)$ (N m) | | | |
| 0.01 | 56.478 | 52.389 | -0.001277 | -0.001083 | -0.001277 | 0.755959 | 1.28 |
| 0.008 | 40.397 | 36.317 | -0.001116 | -0.000961 | -0.001116 | 0.825447 | 1.12 |
| 0.006 | 24.254 | 22.378 | -0.000908 | -0.000781 | -0.000908 | 0.895198 | 0.91 |
| 0.004 | 16.790 | 16.168 | -0.000627 | -0.000539 | -0.000627 | 0.927451 | 0.63 |

(i.e., the exact formulation and the area-averaging approach). It has also been shown (Table III; Eq. (51)), that $\hat{V}_{\theta,o}$ is significantly different from $\bar{V}_{\theta,o}$. Equation (51) implies that, for parabolic velocity profiles, the final results of the mass-flow-averaging approach is as simple as that of the area-averaging approach, differing only by a numerical factor (6/5). The formulation given in Sec. II A for determining the angular momentum in a Tesla turbomachine has, moreover, the following advantages.

First of all, it is a rigorous and generic mathematical formulation. As an example, the present formulation is applicable to incompressible as well as compressible flow; the simple area-averaging approach would be limited to incompressible flow where density does not change appreciably.

Secondly, the present formulation of Sec. II A can deal with flow non-uniformity of arbitrary complexity. As an example, a practical Tesla disc turbine may have one or more discrete nozzles at the periphery, destroying the axi-symmetry of the flow field. The present formulation would be able to tackle such (or any other arbitrarily complex) non-uniformity, whereas the simple area-averaging approach would not be appropriate in such situations.

The example calculations shown in Tables II and III assume that, at inlet, the prescribed tangential and radial velocities are uniform. The implication of having non-uniform (z -dependence) velocities at inlet has been explored in the example calculations shown in Table IV. (Axi-symmetric boundary conditions have been applied at both inlet and outlet for all calculations shown in Tables II–IV.) The cases presented in Table IV are chosen such that $\Delta\bar{H}_o$ is large for all cases. The results show that, even for high values of $\Delta\bar{H}_o$, the difference between mass-flow-averaged and area-averaged formulations can be significant (more so when the inlet conditions are non-uniform).

Thirdly, computation of Γ_{Euler} is not the only objective of the present paper, it also explores several other subtle aspects of the fluid dynamics of work transfer, including its spatial development, in a Tesla disc turbomachine. For example, the complex (sometimes continuous, sometimes disjointed) three-dimensional shapes of the iso-surfaces of $U_{\theta}r$ have been shown, for the first time, in Figures 6 and 7. The radial distribution of the torque potential fraction is investigated in Figures 9 and 10, so that one can determine the amount of torque transfer between any two arbitrary radial positions. The subtle role played by the Coriolis force in the fluid dynamics of work transfer has been elucidated in Sec. IV. Such detailed investigation and understanding of the fluid dynamics of work transfer in the Tesla disc turbomachine would not be possible through the simple area-averaging approach.

Figure 11 shows the spatial development of the percent difference in torque potential ($= 100[(\bar{H}_i - \bar{H}(r)) - (\hat{H}_i - \hat{H}(r))]/[\hat{H}_i - \hat{H}(r)]$, where \hat{H} and \bar{H} denote angular momentum based respectively on the mass-flow-averaging and area-averaging). The figure shows that, because of the large deviations involved, the spatial development of torque and work transfer cannot be studied by the area-averaging technique.

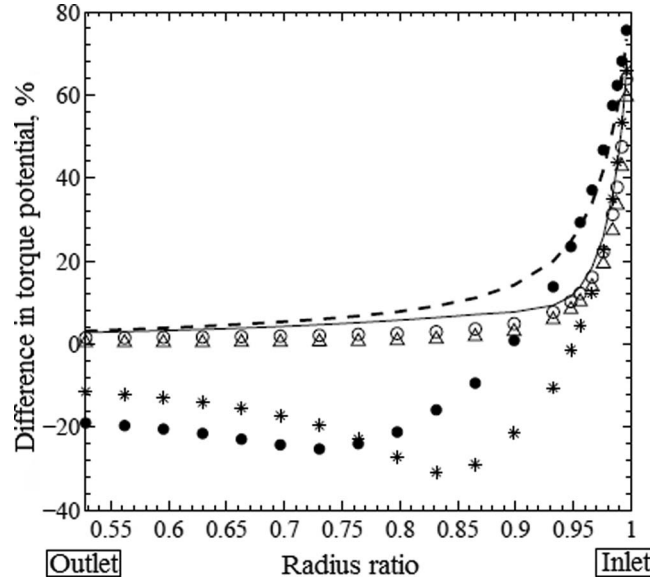


FIG. 11. The spatial development of the percent difference between area-averaged and mass-averaged torque potentials for uniform boundary condition at inlet. [$r_i = 25$ mm ($R = 1$), $r_o = 13.2$ mm ($R = 0.528$), $\bar{U}_{\theta,i} = 106$ m/s, $\bar{U}_{r,i} = -11.5$ m/s, and air is used as working fluid. Keys: • $\bar{b} = 0.0184$, $\phi_i = -0.153$, and $\gamma = 1.413$; * $\bar{b} = 0.0184$, $\phi_i = -0.46$, and $\gamma = 4.24$; ---- $\bar{b} = 0.0092$, $\phi_i = -0.153$, and $\gamma = 1.413$; — $\bar{b} = 0.0092$, $\phi_i = -0.46$, and $\gamma = 4.24$; ○ $\bar{b} = 0.0046$, $\phi_i = -0.153$, and $\gamma = 1.413$; Δ $\bar{b} = 0.0046$, $\phi_i = -0.46$, and $\gamma = 4.24$.]

VII. FURTHER PHYSICAL REFLECTIONS FOR DISC TURBINE

1. When there is no shear stress, $\Gamma_{shear} = 0$. Equation (39) then shows that $\Gamma_{Euler} = 0$. Equation (9) gives $\hat{U}_{\theta,or_o} = \hat{U}_{\theta,ir_i}$. Equation (2) can then be used to transform velocities in the absolute frame to those in the relative frame. This gives

$$\hat{V}_{\theta,or_o} - \hat{V}_{\theta,ir_i} = \Omega (r_i^2 - r_o^2). \quad (59)$$

The LHS of Eq. (59) represents the change in angular momentum in the relative frame and the RHS of Eq. (59) is the specific torque due to Coriolis force. So, in the absence of shear stress, the two parts balance each other.

2. Equation (42) shows that $(\Gamma_{Euler})_2$ will be zero if $(\hat{V}_{\theta,or_o} - \hat{V}_{\theta,ir_i}) = 0$. In this case, the description in the relative frame would be that the torque acting on the control volume is only because of the θ -component of Coriolis force. According to Eq. (53), $(\Gamma_{shear})_2$ is zero when $(\Gamma_{Euler})_2$ is zero. One can then conclude from Eq. (50) that this condition will be achieved when $C_2/C_1 = 1$. In summary, the condition $(\hat{V}_{\theta,or_o} - \hat{V}_{\theta,ir_i}) = 0$ may happen if the fluid properties, disc geometry, and operational parameters satisfy the condition $(|\bar{V}_{r,i}| b^2) / (6(\gamma - 1)\nu r_i) = 1$.
3. $(\Gamma_{Euler})_1$ is always negative. Equation (42) shows that $(\Gamma_{Euler})_2$, however, may become positive if $(\hat{V}_{\theta,or_o} - \hat{V}_{\theta,ir_i}) > 0$. In this case, $(\Gamma_{Euler})_2$ will act opposite to the $(\Gamma_{Euler})_1$ and the net torque will be reduced. The previous condition regarding relative velocities may be satisfied either when $\gamma \geq 1$ (usually when γ is close to 1) or when $\gamma < 1$ (the case of flow reversal in the relative frame of reference). Many possible types of variation in V_θ between the inlet and outlet are discussed in Ref. 14.

Out of all the cases for which $(\hat{V}_{\theta,or_o} - \hat{V}_{\theta,ir_i}) > 0$ is satisfied, one limiting case may arise such that $(\Gamma_{Euler})_1 = -(\Gamma_{Euler})_2$ or, $\Gamma_{Euler} = \Gamma_{shear} = 0$, and therefore the turbine will produce no power output. The condition of no torque can be obtained from Eq. (44) as follows:

$$[\gamma]_{\text{notorque}} = 1 - \frac{10}{6} \left[\frac{C_1 \frac{(1 - R_o^2)}{2} + \left\{ 1 - \exp \left[\frac{C_1}{2} (1 - R_o^2) \right] \right\}}{C_1 \left\{ 1 - \exp \left[\frac{C_1}{2} (1 - R_o^2) \right] \right\}} \right]. \quad (60)$$

4. Guha and Sengupta¹⁴ had shown that under a flow reversal condition in the relative frame of reference $\vec{V}_{\theta,i} < 0$ and $\vec{V}_{\theta,o} > 0$. Now, it has been discussed in Sec. V that $\hat{V}_{\theta,i} = \vec{V}_{\theta,i}$ for uniform velocity profile at inlet and $\hat{V}_{\theta,o} > \vec{V}_{\theta,o}$ at outlet for small disc spacing. Hence, for flow reversal with small inter-disc-spacing ($\hat{V}_{\theta,o}r_o - \hat{V}_{\theta,i}r_i > 0$). This represents a situation when the Tesla disc turbine can generate net torque because of the torque produced by the θ -component of Coriolis force which reverses the direction of V_θ in the direction of the rotation of the discs.
5. When the inter-disc spacing is small so that a parabolic variation of V_θ in the z -direction is a good assumption, the analytical theory described in Sec. III A is valid. Equation (26) can then be recast to show the radial variation in rV_θ :

$$\frac{r\hat{V}_\theta(r)}{r_i\hat{V}_{\theta,i}} = \frac{C_2}{C_1} + \left(1 - \frac{C_2}{C_1}\right) \exp\left[\frac{C_1}{2}\left(1 - \frac{r^2}{r_i^2}\right)\right]. \quad (61)$$

For small inter-disc spacing, Eqs. (58) and (61) can be used to determine (design) the combination of geometrical details and flow input variables for which desirable values of the overall work transfer can be obtained. Equation (58) shows that a low value of $r\hat{V}_\theta$ at rotor outlet is required to achieve a low value of the torque potential fraction at outlet $\Delta\tilde{H}_o$.

The fluid dynamics of the torque and work transfer in a Tesla disc turbine has been examined from several angles in the present paper. The newly defined torque potential fraction has emerged as an important design parameter. There are other important aspects such as the radial pressure drop and efficiency, which have not been presented here to keep the discussion focussed. Equation (14), the radial r -momentum equation, gives the magnitude of pressure drop, and, shows that there are four terms which contribute to the change of pressure—inertial, centrifugal, Coriolis, viscous. Computation of pressure drop and efficiency may be found in Refs. 13 and 14. A similitude analysis and scaling laws for Tesla disc turbomachines are given in Ref. 31. In Ref. 31, it is shown that appropriate scales for non-dimensionalizing the power output and the pressure drop of Tesla disc turbomachines are respectively $\rho |\bar{U}_{r,i}|^3 r_i^2$ (or $\rho\Omega^3 b^5$) and $\rho\bar{U}_{\theta,i}^2$ (or $\rho\Omega^2 b^2$).

VIII. CONCLUSION

The fluid dynamics of work transfer within a Tesla disc turbomachine (turbine or compressor) has been investigated theoretically and computationally. Both the overall work transfer and its spatial development have been considered. It has been established that the work transfer mechanism in a Tesla disc turbomachine is very different from that in a conventional turbomachine, and the formulation of the Euler's work equation for the disc turbomachine (Sec. II) contains several conceptual subtleties because of the existence of complex, three dimensional, non-uniform, viscous flow features within the narrow gaps (of the order of hundred micron) between successive discs. The work equivalence principle, Eq. (11), for this most unusual type of turbomachine involves setting up the equality between the magnitudes of work transfer determined rigorously from two different approaches—one based on the shear stress acting on the disc surfaces and the other based on the change in angular momentum of the fluid. With the help of the Reynolds transport theorem it is shown that mass-flow-averaged tangential velocities (as opposed to the normally used area-averaged values) must be used for an exact determination of the angular momentum, and, the calculation has to be carefully formulated since both radial velocity (that determines throughput) and tangential velocity (that generates torque) depend strongly on the coordinate perpendicular to the disc surfaces (Eq. (5)).

It is shown that both $\tau_{z\theta}$ and $\tau_{r\theta}$ create viscous torque on the fluid (Eq. (10)) and thus need to be considered in a rigorous formulation of work equivalence principle. On the other hand, only $\tau_{z\theta}$ applies on the disc surface and thus only this component is responsible for the transfer of useful power that can be externally extracted from the shaft connected to the discs. It is only if $\tau_{r\theta}$ is negligible that the relation $\dot{W}_x = -\Gamma_{Euler}\Omega$ is strictly valid, where \dot{W}_x is the shaft power output and Γ_{Euler} is given by Eq. (9). The novelty of the analysis of Sec. III B is that Γ_{shear} is determined from the θ -momentum equation without evaluating the term $\partial V_\theta/\partial z$, i.e., a more general analytical

demonstration of the work equivalence principle has been achieved without assuming any specific z -variation of V_θ (such as parabolic profile).

The formulated principle of work transfer has been examined for a disc turbine both analytically as well as computationally, and, in the absolute as well as in relative (rotational) frames of reference. A description of the work equivalence principle in the relative frame of reference shows that torque may be created due to the shear force and Coriolis force. The mathematical analysis automatically leads to a division of both Γ_{Euler} and Γ_{shear} into two parts. The several subtle ways regarding how these two parts of torque may vary (and may reach limiting values) have been discussed. An expression for tangential speed ratio corresponding to the no torque condition [when $(\Gamma_{Euler})_1$ equals $-(\Gamma_{Euler})_2$] has been formulated. The subtle role of $(\Gamma_{Euler})_1$ to produce net power output when flow reversal occurs has been analysed from the mathematical theory as well as from the CFD solutions.

Numerical illustrations given in this paper are for a particular working fluid (air). The results of CFD simulations carried for various values of inter-disc-spacing show that, for smaller disc spacing, iso-surfaces of $U_\theta r$ are continuous surfaces and deviate from the circumferential planes by only a small amount. On the contrary, for larger disc spacings, iso-surfaces of $U_\theta r$ may consist of disjointed surfaces and show complex three-dimensional variations (deviating from the circumferential planes by large extents).

The concept of a new non-dimensional quantity called the torque potential fraction ($\Delta\tilde{H}$) is introduced. The value of $\Delta\tilde{H}$ at the outlet indicates what fraction of the inlet torque potential is actually realized at the particular operating condition. This would be an important design parameter. The value of torque potential fraction at any radial position increases with a decrease in the value of the inter-disc-spacing. It has been observed from the CFD analysis that for small values of \tilde{b} and large values of γ , most of the angular momentum of the fluid is transferred to the surfaces of the discs in the inlet region and correspondingly, the value of $\Delta\tilde{H}$ is very high even in the inlet region. On the other hand, for larger disc spacing, the change of angular momentum in the radial direction is more uniformly distributed between the inlet and the outlet, and the value of $\Delta\tilde{H}$ increases gradually with decreasing radius.

- ¹ N. A. Cumpsty, *Jet Propulsion*, 2nd ed. (Cambridge University Press, Cambridge, 2003).
- ² E. A. Baskharone, *Principles of Turbomachinery in Air-Breathing Engines* (Cambridge University Press, Cambridge, UK, 2006).
- ³ M. P. Boyce, *Gas Turbine Engineering Handbook*, 4th ed. (Elsevier Inc., Waltham, USA, 2012).
- ⁴ S. L. Dixon and C. A. Hall, *Fluid Mechanics and Thermodynamics of Turbomachinery*, 6th ed. (Elsevier Inc., New Delhi, India, 2012).
- ⁵ N. Tesla, Turbine, US Pat. 1061206 (1913).
- ⁶ W. Rice, "An analytical and experimental investigation of multiple-disk turbines," *ASME Trans. J. Eng. Power* **87**(1), 29–36 (1965).
- ⁷ K. E. Boyd and W. Rice, "Laminar inward flow of an incompressible fluid between rotating disks, with full peripheral admission," *ASME Trans. J. Appl. Mech.* **35**(2), 229–237 (1968).
- ⁸ W. Rice, "Tesla turbomachinery," in *Handbook of Turbomachinery*, edited by E. Logan (Marcel Dekker, New York, 2003), pp. 861–874.
- ⁹ G. P. Hoya and A. Guha, "The design of a test rig and study of the performance and efficiency of a Tesla disc turbine," *Proc. Inst. Mech. Eng., Part A: J. Power and Energy* **223**(A4), 451–465 (2009).
- ¹⁰ E. Lemma, R. T. Deam, D. Toncich, and R. Collins, "Characterisation of a small viscous flow turbine," *J. Expt. Therm. Fluid Sci.* **33**, 96–105 (2008).
- ¹¹ A. Guha and B. Smiley, "Experiment and analysis for an improved design of the inlet and nozzle in Tesla disc turbines," *Proc. Inst. Mech. Eng., Part A: J. Power and Energy* **224**, 261–277 (2010).
- ¹² V. P. Carey, "Assessment of Tesla turbine performance for small scale solar Rankine combined heat and power systems," *ASME Trans. J. Eng. Gas Turbines Power* **132**(12), 122301 (2010).
- ¹³ S. Sengupta and A. Guha, "A theory of Tesla disc turbines," *Proc. Inst. Mech. Eng., Part A: J. Power and Energy* **226**(5), 650–663 (2012).
- ¹⁴ A. Guha and S. Sengupta, "The fluid dynamics of the rotating flow in a Tesla disc turbine," *Eur. J. Mech.: B Fluids* **37**, 112–123 (2013).
- ¹⁵ G. K. Batchelor, "Note on a class of solutions of the Navier-Stokes equations representing steady rotationally-symmetric flow," *Q. J. Mech. Appl. Math.* **4**, 29–41 (1951).
- ¹⁶ K. Stewartson, "On the flow between two rotating coaxial disks," *Proc. Cambridge Philos. Soc.* **49**, 333–341 (1953).
- ¹⁷ U. T. Bödewadt, "Die drehströmung über festem grunde," *Z. Angew., Math. Mech.* **20**, 241–253 (1940).

- ¹⁸ S. Poncet, M. P. Chauve, and R. Schiestel, "Batchelor versus Stewartson flow structures in a rotor-stator cavity with throughflow," *Phys. Fluids* **17**, 075110 (2005).
- ¹⁹ M. Holodniok, M. Kubíček, and V. Hlaváček, "Computation of the flow between two rotating coaxial disks," *J. Fluid Mech.* **81**, 689–699 (1977).
- ²⁰ M. Holodniok, M. Kubíček, and V. Hlaváček, "Computation of the flow between two rotating coaxial disks: multiplicity of steady-state solutions," *J. Fluid Mech.* **108**, 227–240 (1981).
- ²¹ A. Guha, "Computation, analysis and theory of two-phase flows," *Aeronaut. J.* **102**(1012), 71–82 (1998).
- ²² A. Guha, "A simple, analytical theory for interpreting measured total pressure in multiphase flows," *ASME J. Fluids Eng.* **120**, 385–389 (1998).
- ²³ A. Guha, "A unified theory for the interpretation of total pressure and temperature in two-phase flows at subsonic and supersonic speeds," *Proc. R. Soc. A: Mathematical, Physical and Engineering Sciences* **454**, 671–695 (1998).
- ²⁴ J. A. Fay, *Introduction to Fluid Mechanics* (MIT Press, Cambridge, MA, 1994).
- ²⁵ G. K. Batchelor, *An Introduction to Fluid Dynamics* (Cambridge University Press, New York, 2005).
- ²⁶ F. M. White, *Fluid Mechanics*, 6th ed. (Tata McGraw-Hill Education, New Delhi, 2008)
- ²⁷ S. Murata, M. Yutaka, and I. Yoshiyuki, "A Study on a disk friction pump," *Bull. JSME* **19**(136), 168–178 (1976).
- ²⁸ R. J. Lingwood, "Absolute instability of the boundary layer on a rotating disk," *J. Fluid Mech.* **299**, 17–33 (1995).
- ²⁹ R. J. Lingwood, "Absolute instability of the Ekman layer and related rotating flows," *J. Fluid Mech.* **331**, 405–428 (1997).
- ³⁰ N. M. M. Cousin-Rittemard, O. Daube, and P. L. Quéré, "Sur la nature de la première bifurcation des écoulements interdisques," *C. R. Acad. Sci. Paris* **326**(6), 359–366 (1998).
- ³¹ A. Guha and S. Sengupta, "Similitude and scaling laws for the rotating flow between concentric discs," *Proc. Inst. Mech. Eng., Part A: J. Power and Energy* (published online).
- ³² C. M. Rhie and W. L. Chow, "A numerical study of the turbulent flow past an isolated airfoil with trailing edge separation," *AIAA/ASME 3rd Joint Thermophysics, Fluids, Plasma and Heat Transfer Conference*, St. Louis, Missouri, AIAA (1982).
- ³³ S. Majumdar, "Role of underrelaxation in momentum interpolation for calculation of flow with nonstaggered grids," *Numer. Heat Transfer* **13**(1), 125–132 (1988).
- ³⁴ Theory Guide of ANSYS CFX 14.5, ANSYS CFX 14.5 (commercial software), ANSYS, Inc., Canonsburg, PA 15317, USA (as of February 2014 available for the licensed user at <https://support.ansys.com/docdownloads>).
- ³⁵ American Society of Automotive Engineers (SAE), "Inlet total-pressure-distortion considerations for gas turbine engines," *Air* 1419 (1983).
- ³⁶ V. D. Romanin and V. P. Carey, "An integral perturbation model of flow and momentum transport in rotating microchannel with smooth or microstructured wall surfaces," *Phys. Fluids* **23**(8), 082003 (2011).